Sedimentary structure discrimination with hyperspectral imaging in sediment cores

Kevin Jacq, William Rapuc, A Benoit, Didier Coquin, Bernard Fanget, Yves Perrette, Pierre Sabatier, Bruno Wilhelm, Maxime Debret, Fabien Arnaud

Sedimentary structure discrimination with hyperspectral imaging in sediment cores

Kévin Jacq[a,b*], William Rapuc[a], Alexandre Benoit[b], Didier Coquin[b], Bernard Fanget[a], Yves Perrette[a], Pierre Sabatier[a], Bruno Wilhelm[c], Maxime Debret[d], Fabien Arnaud[a]

a Univ. Grenoble Alpes, Univ. Savoie Mont Blanc, CNRS, EDYTEM, 73000 Chambéry, France

b Univ. Savoie Mont Blanc, LISTIC, 74000 Annecy, France

c Institute for Geosciences and Environmental Research, University Grenoble Alpes, CNRS, IRD, Grenoble, France

d Univ. Rouen Normandie, Univ. Caen, CNRS, M2C, 76821 Mont-Saint-Aignan, France

Corresponding Author:

Kévin Jacq

UMR CNRS 5204 Environnements, Dynamiques et Territoires de la Montagne (EDYTEM)

Université Savoie Mont Blanc, Campus scientifique,

73376 Le Bourget du Lac cedex, France

jacq.kevin@hotmail.fr

Abstract

Hyperspectral imaging (HSI) is a non-destructive, high-resolution imaging technique that is currently under significant development for analyzing geological areas with remote devices or natural samples in a laboratory. In both cases, the hyperspectral image provides several sedimentary structures that must be separated to temporally and spatially describe the sample. Sediment sequences are composed of successive deposits (strata, homogenite, flood) that are visible depending on sample properties. The classical methods to identify them are time-consuming, have a low spatial resolution (millimeters) and are generally based on naked-eye counting. In this study, we compare several supervised classification algorithms to discriminate sedimentological structures in lake sediments. Instantaneous events in lake sediments are generally linked to extreme geodynamical events (e.g., floods, earthquakes), so their identification and counting are essential to understand long-term fluctuations and improve hazard assessments. Identification and counting are done by reconstructing a chronicle of event layer occurrence, including estimation of deposit thicknesses. Here, we applied two hyperspectral imaging sensors (Visible Near-Infrared, VNIR, 60 µm, 400-1 000 nm; Short Wave Infrared, SWIR, 200 µm, 1 000-2 500 nm) on three sediment cores from different lake systems. We highlight that the SWIR sensor is the optimal one for creating robust classification models with discriminant analyses (prediction accuracies of 0.87-0.98). Indeed, the VNIR sensor is impacted by the surface reliefs and structures that are not in the learning set, which causes mis-classification. These observations are also valid for the combined sensor (VNIR-SWIR) and the RGB images. Several spatial and spectral pre-processing were also compared and enabled one to highlight discriminant information specific to a sample and a sensor. These works show that the combined use of hyperspectral imaging and machine learning improves the characterization of sedimentary structures compared to conventional methods.

Keywords: Hyperspectral Imaging, Machine Learning, Discrimination methods, Visible and Near-Infrared Spectroscopy, Automatic Detection, Sedimentary Deposits

1 Introduction

Natural archives, such as sediment cores, are composed of a succession of deposits, so they record past climate and environment biological-physical-chemical variations. There are two main processes: continuous sedimentation and event layers, and the former can be interrupted by the latter. The continuous sedimentation enables one to create an age-depth model and infer the environment and climate conditions. Event layers, e.g., related to floods (Gaume et al., 2009; Glur et al., 2013), storms (Sabatier et al., 2012), landslides, earthquakes (Wilhelm et al., 2016), tsunamis (Chagué-Goff, 2010), and eruptions, are linked to some of the most damaging disasters in terms of economic and societal losses. Currently, in an overwhelming majority of laboratory studies on natural archives, sedimentary structures are first visually described; subsequently, numerous physical (X-ray imaging, computed tomography scan, grain-size) and chemical (X-ray fluorescence or diffraction, scanning electron microscopy) analyses are undertaken. From those results, the event layers are identified and described. Then, layers with identical characteristics (e.g., color and texture) are usually counted by naked-eye observation. This approach is time-consuming, characterized by a low spatial resolution and subject to high uncertainties due to human interpretation (Lotter and Lemcke, 1999). To overcome these limits, several semi-automatic methods were developed to discriminate these sedimentary deposits from RGB images. The main approaches study the strata from annually laminated sediment to create an age-depth model with their discretization, but they only use a line or a combination of segments, and a deposit is characterized by the detection of the maxima (Meyer et al., 2006; Weber et al., 2010). Similarly, for the automatic detection of event layers, Vannière et al. (2013) proposed to use a 1/Red signal and threshold. Some studies also used discrimination methods based on labeled pixels to create classification maps, e.g., an adaptive neuro-fuzzy inference system (Ebert and Trauth, 2015) or K-nearest neighbor (Ndiaye et al., 2012). Thereby, only the color signal has been investigated, while many other parameters are potentially useful to distinguish event layers, such as the texture, grain size, and chemical composition (Fouinat et al., 2017; Gilli et al., 2013; Wilhelm et al., 2018). A more relevant approach will automatically detect event layers considering all of these parameters.

In the current literature, a great number of works focus on the use of hyperspectral imaging (HSI) data for resource management. For instance, in agriculture applications (Teke et al., 2013) several works are focusing on the analysis of (i) environmental stress in crops and associated diseases (Feng et al., 2017), (ii) crops variability (Rubwurm and Korner, 2017), and (iii) soil erosion stages (Chabrillat et al., 2014) among many others. In forestry and environmental management, relevant works care about analyzing the status and health of forests (Shang and Chisholm, 2014), and infestations in plantation forestry (Peerbhay et al., 2015). In geological exploration and mineralogy, HSI data have been used for detection and mapping of mineral deposits (Contreras Acosta et al., 2019; Dumke et al., 2018) or soil composition analysis (Shi and Wang, 2014). HSI is a non-destructive high-resolution laboratory analysis that enables a semi-automatic description of the natural deposits based on their physical-chemical characterization. HSI can improve chemical knowledge by analyzing the sample surface. It has been used to characterize mineralogical fingerprints (Feng et al., 2018; Lorenz et al., 2019; Tusa et al., 2020b), organic matter (Jacq et al., 2019c; Van Exem, 2018), pigments (Butz et al., 2017; Makri et al., 2020; Schneider et al., 2018), and particle size distribution (Jacq et al., 2019b). Some of these studies highlight sedimentary structures with proxy estimation but without spatially characterizing them. To describe these deposits, image or classification approaches were used with hyperspectral remote sensing imaging (Ghamisi et al., 2017; Li et al., 2019). These approaches have been used in the laboratory for mineralogical characterization of rock cores or for the detection of veins from other sensor data that require destructive sampling (Contreras Acosta et al., 2020, 2019; Tusa et al., 2020a, 2019). These works employ methods such as random forest (RF) or support vector machine (SVM) to classify each hyperspectral pixel into a dominant mineral class or for a mixture of minerals, they used visible and near-infrared (VNIR), short and long wave infrared (SWIR, LWIR) hyperspectral cameras. These approaches are therefore interesting for the problem of detecting sedimentary deposits, but sediments from aquatic environments are moreover more complex than those from rocks because of the presence of moisture and particles that will interfere in the hyperspectral signal (Verpoorter et al., 2014). To this day, only one study based on lake or marine sediments employs HSI to characterize

spatial variations in volcanic tephra layers with a VNIR camera using a supervised classification method based on an artificial neural network and manual non-destructive labeling (Aymerich et al., 2016).

As we have just seen, in the literature many hyperspectral image classification methods have been applied on remote sensing, but few to sedimentary images. Therefore, to classify sediments from cores to know their composition, we want to study three supervised classification methods (decision tree DT, random forest RF, and artificial neural network ANN) and three parametric methods (linear and quadratic discriminant analysis LDA/QDA, partial least-square discriminant analysis PLS-DA). These six methods are problematically specific (Khaledian and Miller, 2020). The hyperspectral images used in this study come from a visible and near-infrared camera (VNIR, pixel size: 60 µm) and a shortwave infrared sensor (SWIR, pixel size: 200 µm). The two sensors can also be combined to estimate a VNIR-SWIR composite sensor (pixel size: 200 µm) or reduced to create composite RGB images. Several spectral and spatial pre-processing and compression algorithms were compared. Thus this study proposes to compare numerous approaches (the type of image, pre-processing, and discrimination) to separate and characterize the sedimentary structures of three different samples and provide a simplified methodology for its application to other sites.

2 Materials and methods

2.1 Sample site descriptions

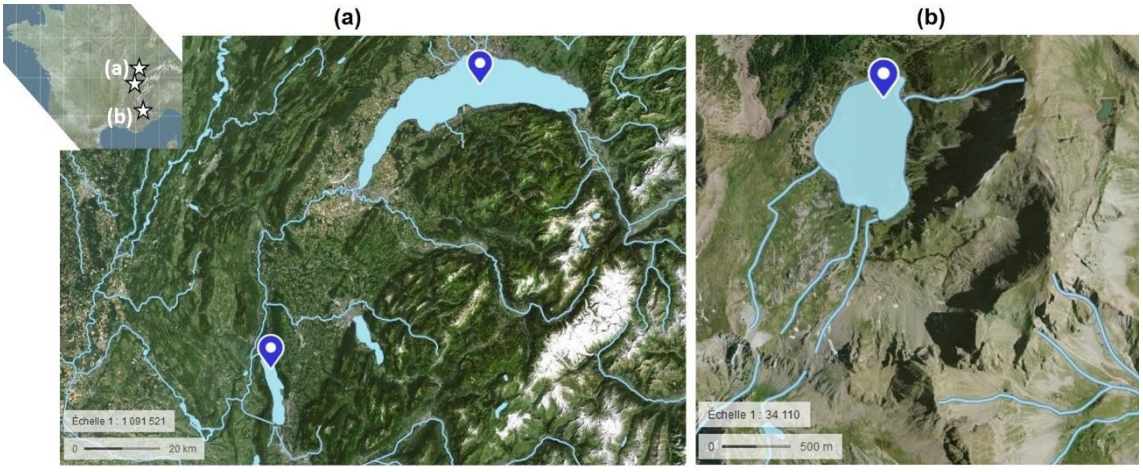

Figure 1: Locations, tributaries, and effluents of the lakes: (a) Bourget and Geneva, (b) Allos

Three sediment cores were selected from three lakes located in the western French Alps (Figure 1) in different watersheds, representing different geological contexts and surface areas that present event layers with different geochemical compositions. The studied cores were retrieved from Lake Allos (ALO09_P13, IGSN: IEFRA08JN, coring year: 2009) (Wilhelm et al., 2015, 2012), the deep basin of Lake Le Bourget (LDB17_P11, coring year: 2017, water inflow: 10.65 $m.an^{-1}$) (Jenny, 2013; Jenny et al., 2014), and Lake Geneva (LEM10_P6, IGSN: IEFRA008N, coring year: 2010, water inflow: 13.07 $m.an^{-1}$) (Jenny, 2013; Rapuc et al., 2020).

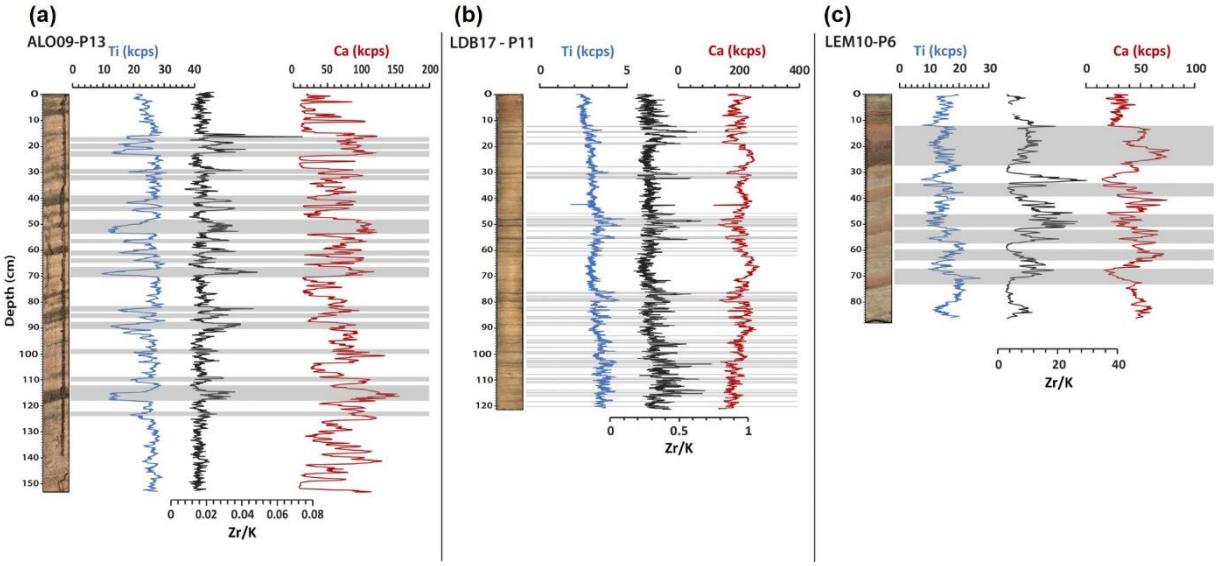

Figure 2: XRF analysis for Ti, Zr/K, and Ca of the three cores: (a) Allos, (b) Bourget, and (c) Geneva

The sediment from the three selected cores was first described and logged after naked-eye observations. When they were present, the event layers were distinguished from the continuous sedimentation by using sedimentological and geochemical results; for these three cores X-ray fluorescence, particle size distribution, and total organic carbon were made.

Lake Allos sediment sequence (ALO09_P13) presents two different sedimentary units. The upper part is enriched in organic matter and presents Total Organic Carbon (TOC) values > 1.5% (Wilhelm et al., 2012). The rest of the sequence is composed of light-gray homogeneous silty clay (median = 10 µm),

corresponding to the continuous sedimentation, which is interrupted by coarser (median = 40 µm) normally graded beds (Wilhelm et al., 2012). These beds present higher values of dry bulk density, lower TOC values (< 1%), and are enriched in calcium contents (Figure 2). XRF signals also show peaks of Zr/K and low Ti values due to an increase of the grain size at the base of the layers and a depletion in silicate particles, respectively. The graded beds were interpreted as linked to turbidity currents triggered by gravity reworking or flood events (Wilhelm et al., 2012).

Lake Bourget sediment sequence (LDB17_P11) presents two main units. The first one (0-10 cm) is laminated with an alternation of white/light-gray and dark-gray/brown laminae. These laminae are mainly composed of diatoms, micrite, organic matter (TOC > 2.5%), and autochthonous calcite with a mean grain size comprise between 15 and 30 µm (Giguet-Covex et al., 2010). The second unit is non-laminated and corresponds to homogeneous light-gray sediment composed of carbonate particles, silts, clays, and a few diatoms. The mean grain size of this unit is almost constant and is comprised between 4 and 9 µm. The organic matter content is under 5% (Giguet-Covex et al., 2010), and carbonate particles represent at least half of the total sediment (Arnaud, 2005). Several darker deposits, enriched in detrital silicate and carbonate particles, interrupted the continuous sedimentation and were interpreted as underflow deposits linked to flood events (Giguet-Covex et al., 2010; Jenny et al., 2014). These deposits present peaks of Ti and Zr/K signals at their base (Figure 2), which support the higher detrital content and the increase of grain size within these layers.

Like the two other sediment sequences, the Lake Geneva sequence (LEM10_P6) presents two principal sedimentary units. The upper laminated unit corresponds to an alternation of light and dark-gray laminae, enriched in organic matter (TOC values > 5%; (Jenny, 2013)). This unit is followed by homogeneous light-gray silty clay identified as a non-laminated unit (Jenny, 2013), which presents lower organic content (TOC values < 2%) and higher values of calcium (Figure 2). The mean grain size of these two units is higher (> 25 µm) than Lake Bourget sediment sequence values. The lower unit is interrupted by thick and coarse graded beds that show peaks of Zr/K, and higher values of Ti (Figure 2)

155 are linked to increased detrital silicates compared to the continuous sedimentation. These deposits
156 present similarities with those observed in the two other sequences and were interpreted as flood
157 layers.

158 Once clearly identified, those layers were visually counted. The data sets will be referred to using the
159 name of the lake, but it must be understood that there may be differences (color, chemical, physical)
160 among different sequences from the same lake.

161 2.2 VNIR and SWIR hyperspectral image acquisition

162 Two hyperspectral reflectance cameras were used to analyze these cores at the UMR CNRS M2C lab
163 facilities, University of Normandie-Rouen (France). They cover two consecutive spectral ranges: 400-1
164 000 nm (visible and near-infrared, Specim VNIR PFD OLE23) and 968-2 574 nm (shortwave infrared,
165 Specim SWIR OLES22.5). They have a theoretical spatial pixel size of 60 µm and 200 µm, respectively.
166 The real resolution may vary due to surface roughness. Relevant data were obtained with a flattening
167 and a cleaning of the core to have a plane surface that revealed sediment structures (Butz et al., 2015;
168 Jacq et al., 2020). Then, the camera was calibrated with a spectral acquisition on a reference, as the
169 image of a known object has squared pixels (true shape) and relevant reflectance intensities (color and
170 signal-to-noise ratio).

171 The resolution of the two datasets (VNIR and SWIR) was also homogenized at a common spatial
172 resolution of 200 µm to obtain a VNIR-SWIR composite sensor. The two hyperspectral images were
173 combined into a unique one (i.e., VNIR-SWIR) with image registration (Liu et al., 2011) adapted to HSI
174 on a wavelength plane characteristic of a similar chemical compound. In previous work, we found that
175 the 970 nm (VNIR) and 1 200 nm (SWIR) wavelengths were optimal for combining (Jacq et al., 2019a).
176 They are related to hydroxyl chemical bonds mostly associated with moisture in sediment cores (Bull,
177 1991; Viscarra Rossel and Behrens, 2010). Therefore, a composite sensor was created to merge the
178 VNIR and SWIR datasets to cover the range of 400-2 500 nm. No reflectance adjustment was used to
179 correct for shifts in the spectral overlap range between the two sensors. In this study, we compare the

classification performances of three datasets: VNIR at a spatial resolution of 60 µm, SWIR at a resolution of 200 µm, and VNIR-SWIR at a resolution of 200 µm.

Pre-processing can be used to correct the data from noise or aberrant values and highlight discriminant wavelengths. The three dimensions of the HSI, spectral, and spatial pre-processing procedures can be used (Rinnan et al., 2009; Vidal and Amigo, 2012). The spectral pre-processing procedures compared in this study are normalization (autoscale), linear baseline correction (detrend), scattering effect correction (Standard Normal Variate (SNV) and Multiplicative Scatter Correction (MSC)) (Barnes et al., 1989), and Savitzky-Golay first and second derivatives (D1 and D2) (Savitzky and Golay, 1964). The derivatives use second-order polynomial fitting and a window of 7 and 13 wavelengths for the first and second derivatives respectively. Principal component analysis (PCA) was also used as a compression of the spectral dimension (Pearson, 1901). Contrast limited adaptive histogram equalization (CLAHE) was used on the spatial dimensions with an estimation based on the grayscale image levels and applied to each image wavelength (Zuiderveld, 1994). Thus, nine datasets per sensor were used for training in an independent way.

2.3 Data Analysis

Six commonly used machine learning algorithms were used to create classification models with three types of spectral data (VNIR, SWIR, and VNIR-SWIR) (Figure 3). First, an RGB image was made from the VNIR HSI to visually and manually label continuous sedimentation and event layer pixels by an expert. Then, machine learning methods were used to construct discrimination models. In addition, nine pre-processing procedures (spatial and spectral) were used and compared with raw data. Consequently, 162 discriminations models were created for each sample to find the optimal sensor (of three), method (of six), and pre-processing procedure (of nine) as presented in Figure 3.

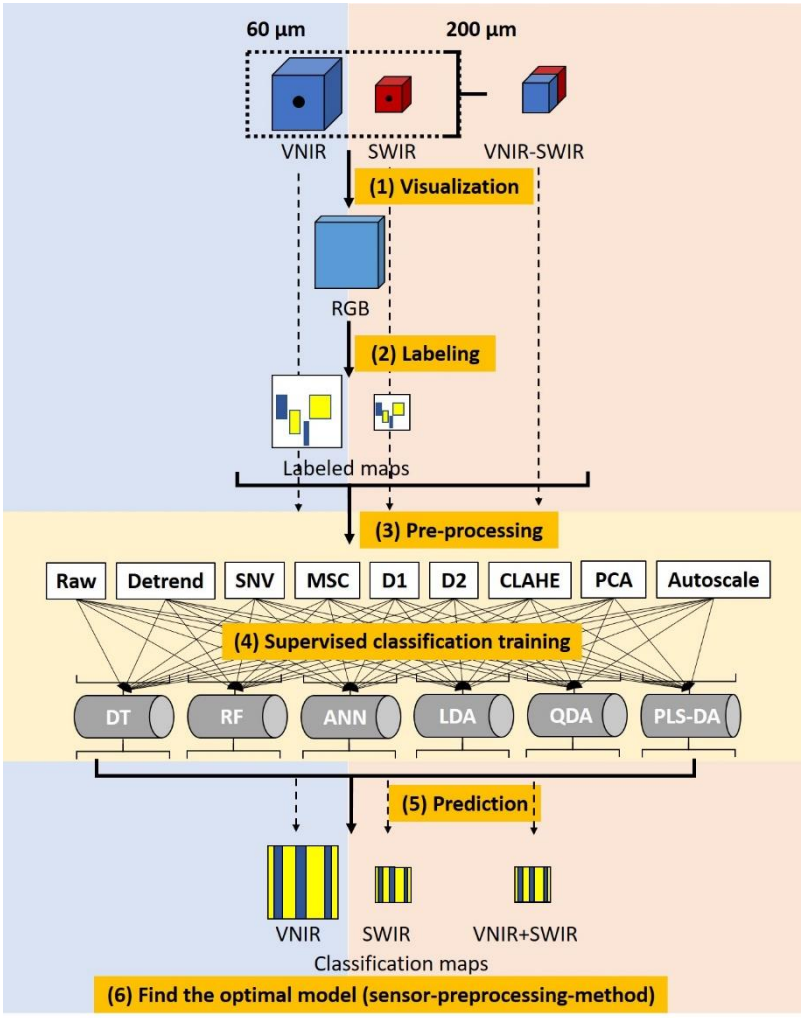

Figure 3: Data processing to create a classification model to predict each pixel: (1) Visualization with RGB images at both resolutions; (2) Manual labeling of the image; (3) Data pre-processing and (4) Creation of supervised classification models for each dataset (DT: Decision Tree, RF: Random Forest, ANN: Artificial Neural Network, LDA: Linear Discriminant Analysis, QDA: Quadratic Discriminant Analysis, PLS-DA: Partial Least Squares Discriminant Analysis); (5) Prediction for each image; (6) Estimation of the optimal model depending on the sensor, pre-processing procedure, and discrimination model

2.3.1 Data labeling

Hyperspectral VNIR data can be reduced to three planes that correspond to a Red-Green-Blue image from the VNIR sensor (611-549-464 nm, according to the RGB standard) (CIE, 1999). The RGB images are representation modes adapted for naked-eye assessment and were used to visualize the sample to label the sedimentary structures. Thus, the user must manually select rectangular areas that correspond to the different studied classes based on the known deposits characterized by

geochemical, textural, and mineralogical analysis. The resulting maps were used as a mask with 0 values for non-labeled pixels and other values for labeled pixels (1: event layer, 2: continuous sedimentation). It was also used to extract the labeled pixels and their corresponding spectrum (Figure 4). For the SWIR dataset, these maps were also made with VNIR data at 60 µm and resized at 200 µm.

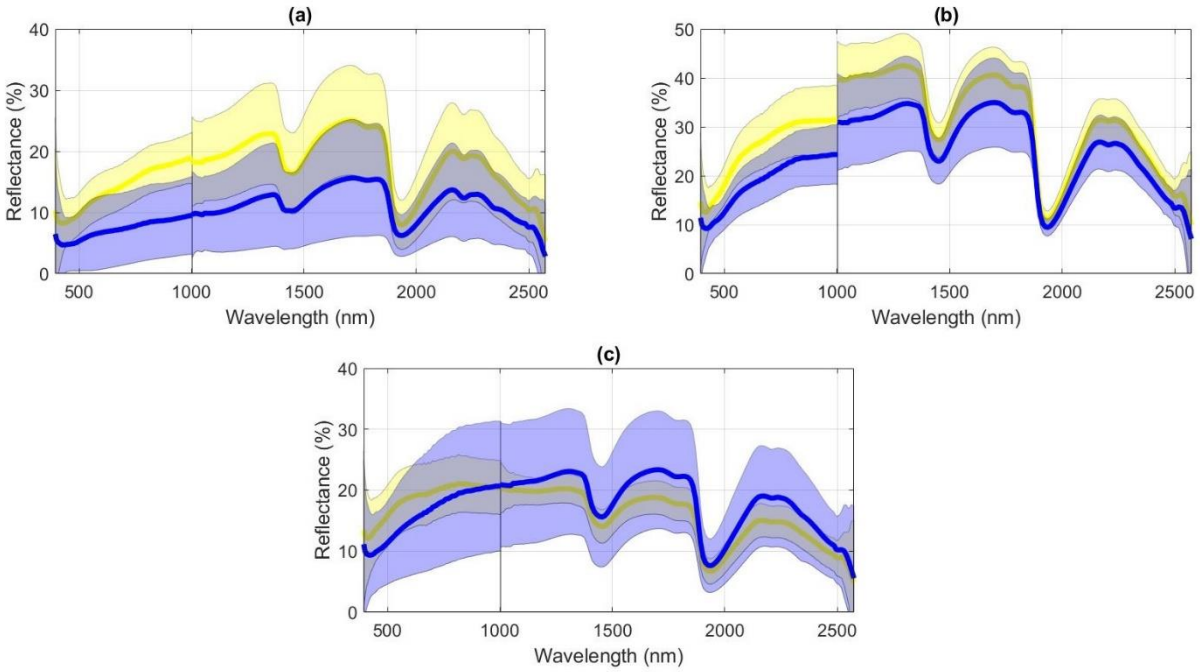

Figure 4: Spectral variations of labelled pixels for each class (blue = event layers; yellow = continuous sedimentation) and for the three cores: (a) Allos, (b) Bourget and (c) Geneva. The reflectance of the sediments depends on the specific sedimentary properties of the sites studied. It seems difficult to visually estimate specific discriminating spectral areas of the two classes studied, therefore statistical approaches will allow to find the discriminating variations

2.3.2 Classification modeling

Several methods commonly used in the literature were chosen for comparison because there is no universal method (Khaledian and Miller, 2020). Six methods were used to create a supervised classification model to discriminate the two sedimentary processes (Figure 5, Supplementary table 1).

Decision trees are a rule-based approach to classification and regression problems (Breiman et al., 1984). They use the values in each feature to split the dataset to a point where all data points that

have the same class are grouped together. A tall tree with multiple splits generates better classifications.

The random forest is a classification algorithm consisting of many decisions trees (Ho, 1995). It uses bagging and features randomness when building each individual tree to try to create an uncorrelated forest of tree whose prediction by committee is more accurate than that of any individual tree.

ANN is a set of connected input-output network in which weight is associated with each connection (Ivakhnenko and Lapa, 1965; McCulloch and Pitts, 1943; Rosenblatt, 1958). It consists of one input layer, one or more intermediate layers, and one output layer. Learning of neural network is performed by adjusting the weight of connection. By updating the weight iteratively performance of the network is improved. During training, the interconnection weights are optimized until the network reaches the specified level of accuracy. It has many advantages like parallelism, less affected with noise, good learning ability

Linear discriminant analysis (LDA) is a straightforward method applying the generative approach for classification (Fisher, 1936). It is based on the assumption that each class can be modeled by a Gaussian distribution and that all the classes share the same covariance matrix. In practice, LDA requires few computations to estimate the classifier parameters that amount to computing percentages and means, plus a matrix inversion.

Quadratic discriminant analysis (QDA) is similar to LDA but without the assumption that the classes share the same covariance matrix, i.e., each class has its own covariance matrix (Fisher, 1936). In this case, the boundary between classes is a quadratic surface instead of a hyperplane.

Partial least squares-discriminant analysis (PLS-DA) is a versatile algorithm that is used for predictive and descriptive modeling as well as for discriminative variable selection (Wold et al., 1984). However, versatility needs to optimize a wealth of parameters before reaching reliable and valid outcomes.

Khaledian and Miller (2020) propose to consider different properties to define the optimal approach to answer the problem. These methods are based on common or specific assumptions as presented briefly above. Some require a large amount of data, such as ANN, while others are less sensitive to sample size. The computation time is also related to the amount of data, as well as to the complexity of the problem, the number of iterations, and the adjustments. Some are easily interpretable (DT, LDA, QDA, PLS-DA), or complex (RF, ANN with few neurons), and some are "black boxes" (ANN with many neurons). Here we use the ANN with few neurons to prioritize the spectral interpretability. Some require the user to define hyperparameters that are presented in Supplementary table 1. Thus, these different methods were chosen to see the effect of these properties on the different datasets (sensors, pre-processing) in predicting the two sedimentary deposit types for the three different sites.

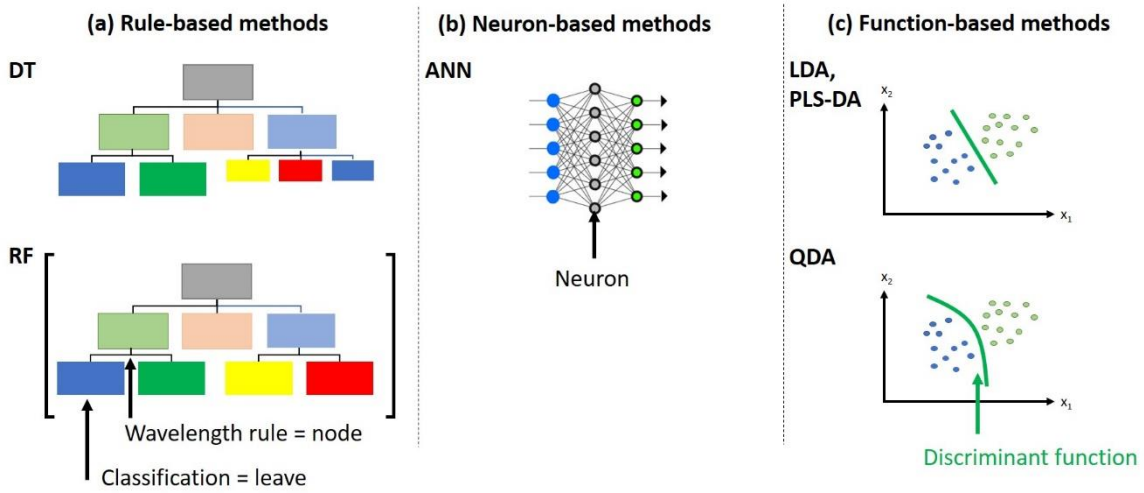

Figure 5: Schematic representation of the machine learning methods used in this study depending on their basis: (a) rules; (b) neurons; and (c) functions

The models were fitted with a randomly selected 70% of the data during calibration, and the remaining data were used in the test set (Supplementary table 2). This ratio was applied to the class with fewer labeled pixels to have a consistent number in each group in the calibration step. The same calibration and test sets were used for each classification method, but they were different for each pre-processing procedure. The labeled pixel number depends on the ability of the user to precisely see the deposits; then, only pixels that certainly belong to these classes are labeled to avoid introducing uncertainty by

uncertain labeling. Due to the compression of the labeled high-resolution map, the pixels of the contours may have been removed as being uncertain, which slightly changes the labeling percentages between the two resolutions. That change explains the difference between the cores with labeled pixels of between 0.45% and 15.71% for one class It also allows visualization of the learning capacity depending on the number of calibration pixels. 5% of the Allos lake image was labeled, against 1.1% for the Bourget lake or 16% for the Geneva lake.

2.3.3 Quantitative and qualitative assessments of model classification

The quantitative performances of the classification models were estimated by the overall accuracy, precision and recall in calibration and prediction:

$$Accuracy = \frac{True\ positive + True\ negative}{True\ positive + True\ negative + False\ positive + False\ negative} \quad (1)$$

$$Precision = \frac{True\ positive}{False\ positive + True\ positive} \quad (2)$$

$$Recall = \frac{True\ positive}{False\ negative + True\ positive} \quad (3)$$

Given a classifier and an instance, there are four possible outcomes. If the instance is positive and it is classified as positive, it is counted as a “true positive”; if it is classified as negative, it is counted as a “false negative”. If the instance is negative and it is classified as negative, it is counted as a “true negative”; if it is classified as positive, it is counted as a “false positive”.

The overall accuracy is the proportion of correct predictions (both “true positives” and “true negatives”) among the total number of cases examined. The precision corresponds to the fraction of first class correct predictions (only “true positives”) among the retrieved first class. The recall is the fraction of relevant first-class predictions that were retrieved. Thus, a value closer to 1 indicates better predictive ability.

Once a model is considered relevant, it is used on each pixel of the hyperspectral image to classify them and estimate a classification map. An expert must then visually and qualitatively evaluate its

spatial coherence, using the different successive deposits and its noise level. Hence, a qualitative index with values between 0 and 5 (arbitrary) is used. A value of 0 corresponds to an irrelevant classification map induced by a model that cannot generalize (under or over-fitting); a value of 5 shows globally relevant classifications on the whole image; whereas a value in this interval indicates more or less relevant predictions but with defects (noise, mispredicted deposits). Moreover, it is important to understand the models on the importance they give to different wavelengths. Complex models like RF and neural networks with a large number of neurons are not easily interpretable.

3 Results and interpretations

3.1 Comparison of the classification methods and pre-processing procedures

Nine pre-processing procedures were tested on each sample, each sensor, and each discrimination method to find the optimal combination (Figure 6). As shown in Figure 4, the spectra of the two classes overlap partially or totally, so the pre-processing step must highlight the wavelengths with discriminating variations to create performant and robust models. PCA and second derivatives (D2) had the lowest prediction accuracies for each sensor and sample (Figure 6). The PCA reduction may not maintain the discriminant information in the main PCs and D2. Raw, CLAHE, autoscaled, and detrended data had the highest discriminant properties in all cases (Figure 6). Some pre-processing procedures are sensor-dependent, such as SNV and MSC, which presented low accuracy for the VNIR sensor and high accuracy for the SWIR sensor. The first derivative (D1) had intermediate accuracy for all cases except for the SWIR sensor and Allos sample, for which good performances were obtained.

Among the discriminant methods, DT had the lowest prediction accuracy in most cases, whereas ANN, QDA, and RF had the highest accuracy. For the ANN, few neurons (2-3) appeared to be better than more neurons. The latter has many more parameters and may overfit the small amount of training data, which limits its generalization capability on the test set. The accuracies of the optimal methods are close and must be discussed with all quantitative values and interpretations of their discriminant

spectral properties. It is important to consider that the results are sample- and site-specific.

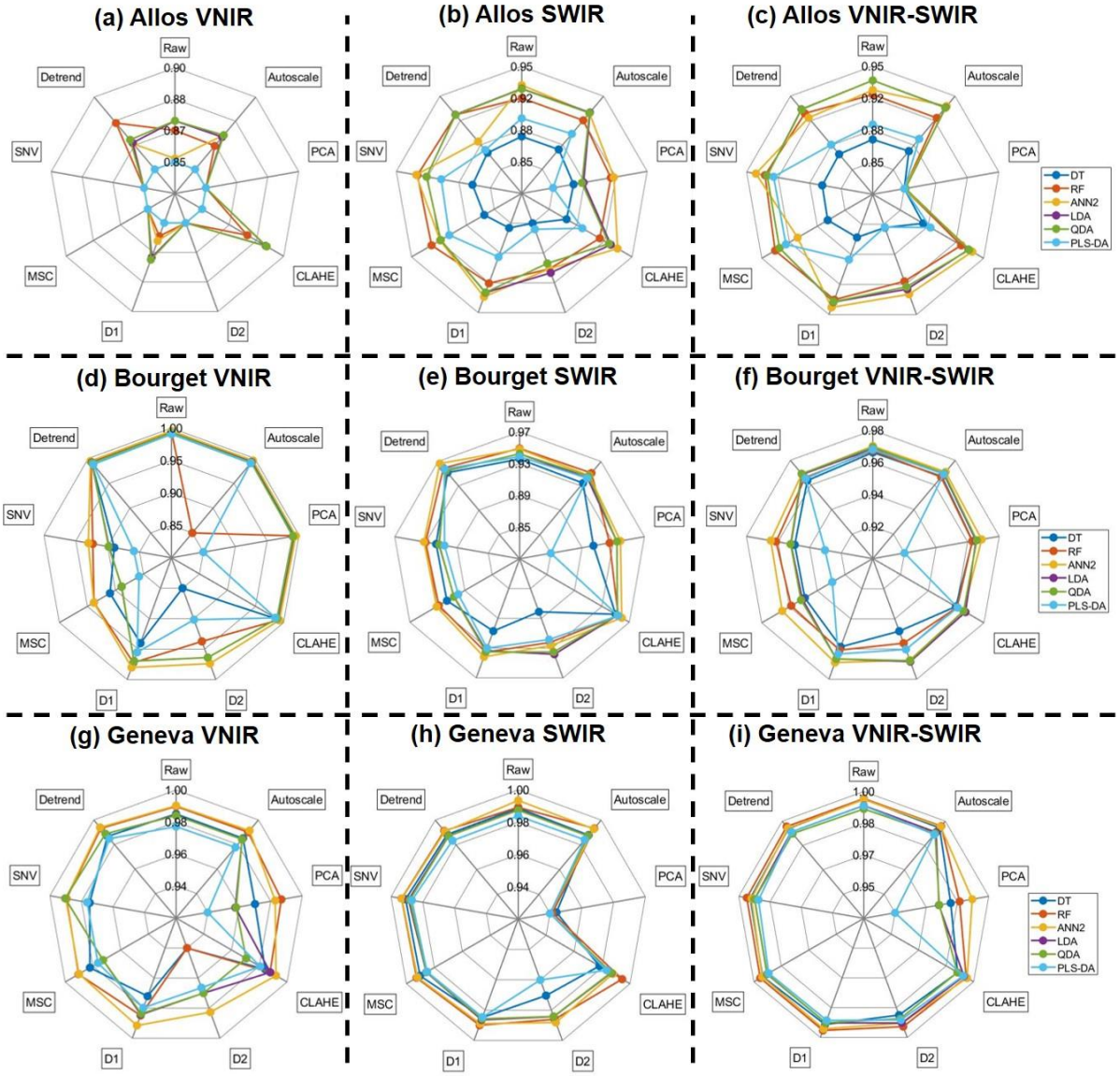

Figure 6: Radar charts of the impact of pre-processing on the overall prediction accuracy of each classification method and lake core hyperspectral image (a-c: Lake Allos; d-f: Lake Bourget; g-i: Lake Geneva; a, d, g: VNIR sensor; b, e, h: SWIR sensor; c, f, i: VNIR-SWIR sensor)

3.2 Optimal models for each image type

The calibration and prediction accuracies, precisions and recalls of the optimal models were higher than 0.8 and mainly 0.9, which highlights the presence of spectral discriminant information in both sensors (Table 1, Supplementary table 3Supplementary table 5). Nevertheless, it also highlights that the best discriminant capacity derived from the SWIR sensor and therefore the VNIR sensor does not

328 contain as much discriminating information. The combination of the two sensors, which should present
329 a better discriminant capacity through the greater amount of spectral information, presents an
330 intermediate discriminant ability. Thus, the predictions are certainly biased by some VNIR data
331 variations.

332 Among all the models developed, some observations have been made (Supplementary table 3-
333 Supplementary table 5). ANNs with two neurons are often the optimal discriminant method based on
334 the prediction accuracy and parsimonious because adding neurons does not improve the accuracy.
335 However, for the qualitative index, discriminant analysis methods (LDA, QDA, PLS-DA) generally had
336 the best performance levels. The computation time is lower for the LDA, PLS-DA, and DT methods, and
337 all of these methods are fast to compute, so the computation time was not used to select the optimal
338 model. It is also more important when there is more data to learn which is the case for the Allos section
339 compared to the others. Based on a compromise between these two first properties (quantitative and
340 qualitative index), the optimal methods in most cases were LDA or PLS-DA. Table 1 highlights an
341 optimal pre-processing procedure that mainly depends on the sample. The discrimination methods
342 appear to have had a low impact on it, which suggests that an optimal pre-processing procedure can
343 highlight the discriminant wavelengths.

344 Table 1: Optimal models for each sample and based on the parameters indicating their performance and robustness

345

Site	Allos	Bourget	Geneva
Sensor	SWIR	SWIR	SWIR
Method	PLS-DA	PLS-DA	LDA
Processing	SNV	Detrend	SNV
$Accuracy_{cal}$	0.900	0.969	0.992
$Precision_{cal}$	0.908	0.988	0.996

$Recall_{cal}$	0.890	0.951	0.989
$Accuracy_{pred}$	0.902	0.958	0.989
$Precision_{pred}$	0.785	0.996	1.000
$Recall_{pred}$	0.885	0.949	0.989
Qualitative	5	5	5
Computation time (s)	0.800	0.219	0.113

346

347 The classification map comparison of the optimal and worst models highlights that the VNIR sensor is
348 more sensitive to surface reliefs, as observed in Figure 7.a-b with fissures and holes due to sampling
349 or Figure 7.d-e with shadows. Darker laminated areas are noticeable on the Bourget and Geneva
350 sediment sections (on the left of the picture), which were not initially labeled because of the non-
351 possibility of precisely labeling the two classes. In these areas, the VNIR sensor predicted that most of
352 the pixels in the event layer class might be due to the similar color with this class. In contrast, the SWIR
353 data correctly predicted the two groups due to the additional spectral discriminant information. For
354 the Allos sediment section (Figure 7.a-c), the event layers are easily distinguishable from the
355 continuous sedimentation due to their darker colors. However, there is also a color gradient linked to
356 a grain size gradient that is spectrally registered in the SWIR range (Jacq et al., 2019b), which explains
357 the wider layers estimated from the SWIR data than from the VNIR data, and the lightest layers are
358 not visible with the VNIR data.

359 All of these observations and the quantitative validation are consistent with the greatest discriminant
360 capacities being associated with the SWIR sensor for separating event layers from continuous
361 sedimentation. Thus, the combination of the two sensors is not better, as we expected due to the VNIR
362 data sensitivity to surface roughness, and the combination will not be used further.

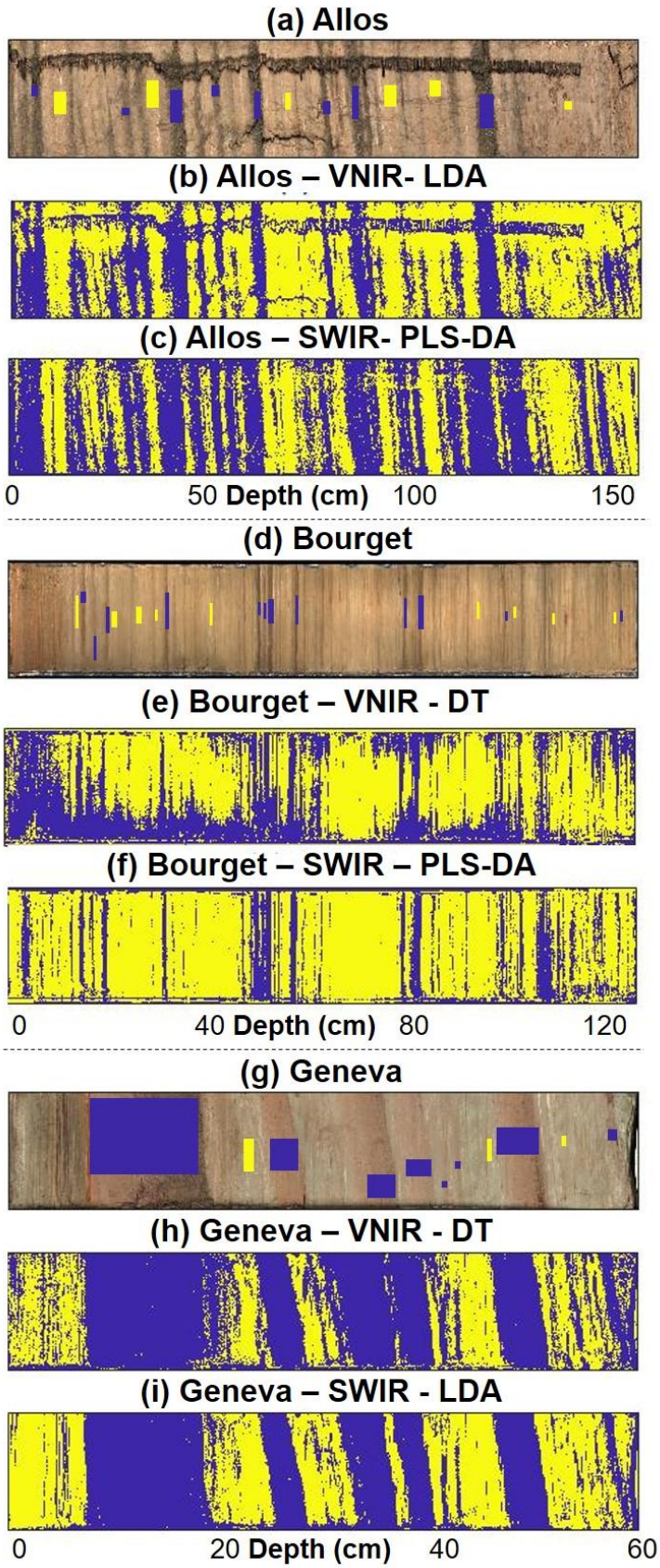

363

364 Figure 7: Optimal (c, f, i) and worst (b, e, h) models for each sediment core sample (a, b, c: Allos; d, e, f: Bourget; h, i, j:

365 Geneva) and labeled areas (blue = event layers; yellow = continuous sedimentation)

3.3 Spectral signatures

Figure 4 shows the spectra corresponding to the two classes. For lakes Allos and Bourget, both classes partially overlap, and the event layers show a lower reflectance that can be due to a darker color of the layers. The overlap is more important for Lake Geneva. The color of the sediment is obviously dependent on the sedimentary properties that are specific to the study sites. It is therefore difficult to visually estimate discriminating spectral areas.

The different statistical approaches used will allow to estimate automatically the spectral areas allowing to separate the two classes. The estimation of SWIR wavelength cumulative occurrence allows to identify the discriminant wavelengths and to characterize them (Figure 8). It is interesting to observe that the five approaches discussed in this figure show similar discriminating spectral areas, which indicates that despite their differences they can adapt to the problematic. Five main discriminant spectral areas present high cumulative values and can be associated with chemical properties. Organic components can be related to spectral wavelengths between (1) 1 050-1 200 nm and (2) 1 650-1 750 nm (Cloutis, 1989; Viscarra Rossel and Behrens, 2010). The three others correspond to spectral ranges with possible overlaps: (3-4) organic compounds and hydroxyl bonds (moisture, organic matter or mineral) between 1 350-1 500 nm and 1 800-1 950 nm, and (5) mineral (clay) and organic compounds between 2 150-2 300 nm (Krupnik and Khan, 2019; Verpoorter et al., 2014; Viscarra Rossel and Behrens, 2010).

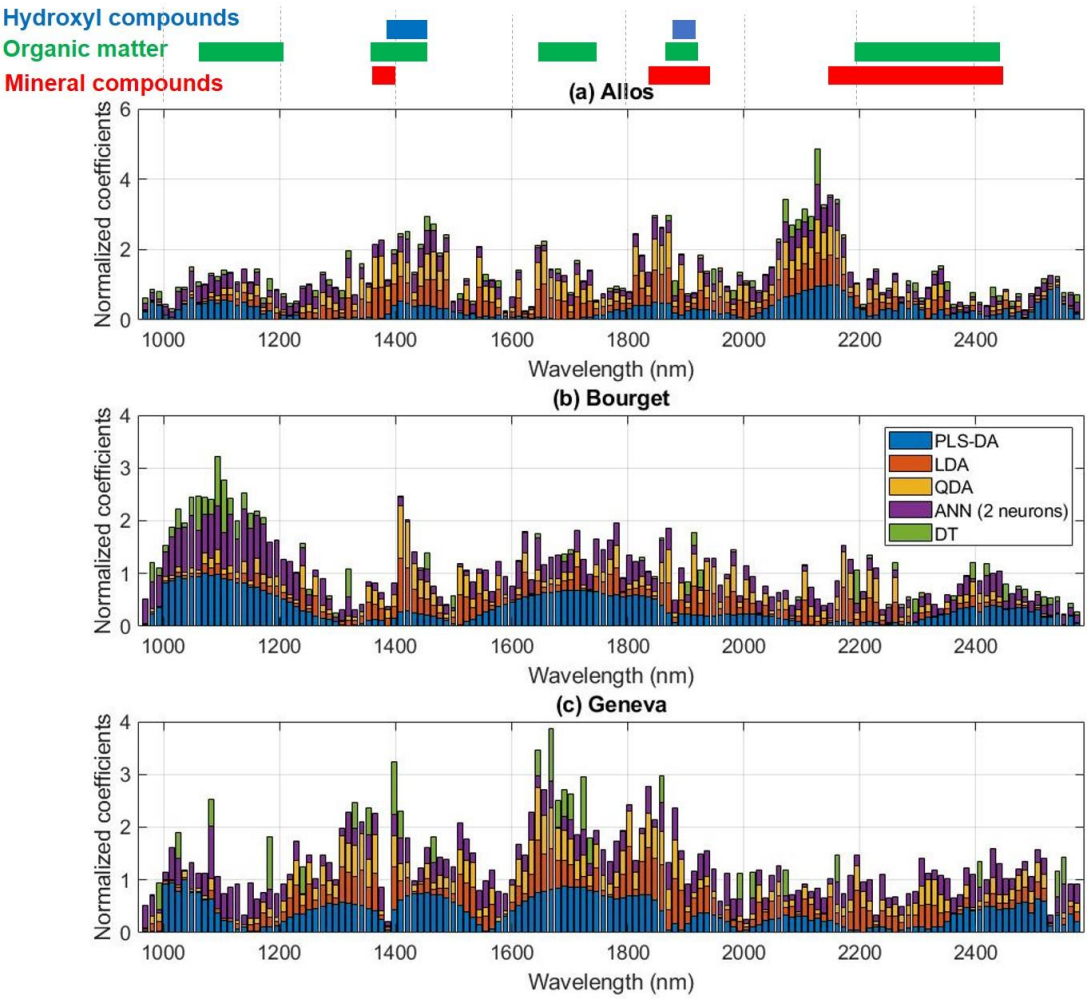

384

385 Figure 8: Comparison of the normalized coefficients (coefficient weights normalized to one for each method) used by the
386 optimal SWIR models to highlight the discriminant wavelengths: (a) Allos, (b) Bourget, and (c) Geneva samples

387 The three optimal core models use similar discriminant wavelengths but have different importance
388 depending on the sediment properties. The two hydroxyl bond spectral areas have important
389 implications in the three models and could be due to interstitial moisture that may be associated with
390 coarser particles present in the event layers. The model estimated for Lake Allos highlights another
391 spectral area characteristic of clays (2 150-2 200 nm) associated with continuous sedimentation.
392 Whereas Lake Bourget and Lake Geneva models use specific areas of organic matter (1 050-1 150 nm,
393 1 350-1 400 nm, 1 650-1 750 nm) due to higher organic matter concentration in both sediment
394 sequences. Thus we can see that the SWIR sensor allows to highlight several sedimentary properties

that can differentiate the two types of deposits. It should be noted that the sedimentary properties highlighted differ and are dependent on the studied site.

4 Discussion

4.1 Generalization of the model on the other sites

Optimal SWIR models developed on each core were used to produce the classification maps of the other cores and to observe the model generalization capability. Table 2 and Supplementary figure 1 show the results of these classifications with the test accuracies and qualitative indicators. Most of the models agree on the difficulty of generalizing the model to other cores, which is explained by the differences in reflectance and thus in sediment composition of the sediment sequences as shown in Figure 4. As the continuous sedimentation of Lake Bourget and Lake Geneva is more organic than the one of Lake Allos, or the granulometry and interstitial humidity allowing to trace textural changes in the event deposits that are more significant for Lake Allos than the other. Unfortunately, mineralogical changes (silicates and carbonates) do not show marked absorptions in the spectral domains studied. Only the model developed with the Bourget data could estimate the classification maps for the other cores, possibly since it has less spectrally localized discriminant wavelengths than the other two models (Allos: 2 100-2 200 nm; Geneva: 1 650-1 700 nm).

Table 2: Comparison of site-specific models for the generalization to the other cores

			Samples		
			Allos	Bourget	Geneva
Models	Allos	$Accuracy_{pred}$		0.367	0.043
		Qualitative		0	0
	Bourget	$Accuracy_{pred}$	0.973		0.365

		Qualitative	3		1
	Geneva	$Accuracy_{pred}$	0.433	0.644	
		Qualitative	0	0	

Based on these results, the estimation of a classification model is sample-specific. It can be made with a linear discriminant method such as LDA or PLS-DA with the raw SWIR dataset, even if some pretreatment slightly improves the performance.

4.2 Event layer classification with classical images

The true RGB image can also be converted into HSV (Hue, Saturation, Lightness) or L*a*b* (lightness, color) color spaces and reduced to a grayscale level. The HSV and L*a*b* transformations have been proven to be more adaptable for classification purposes (Bora et al., 2015; Hernández-Hernández et al., 2016). The grayscale levels are the most straightforward color space.

Table 3 and Supplementary figure 2 show that the conventional image presents slightly lower performances with the VNIR data and has the same mispredictions in terms of surface variations, shadows, and laminated areas (Supplementary table 3). All of these observations highlight that these methods learn the color of the deposits too well with VNIR data and do not learn enough from the chemical composition. Then, machine learning and a conventional image can be used in the case of a clean image and sample with only color differences between the classes and learning of all types of sample events and defects.

Table 3: Comparison of the conventional image discriminant models with the optimal predictions being estimated by the hyperspectral images

Sample	Performance	Grayscale	RGB	HSV	L*a*b*	VNIR HSI	**SWIR** **HSI**
Allos	Method	ANN – 2 neurons					**PLS-DA**

	$Accuracy_{cal}$	0.966	0.821	0.817	0.821	0.889	**0.900**
	$Accuracy_{pred}$	0.963	0.824	0.808	0.823	0.890	**0.902**
	Qualitative	4	4	4	4	3	**5**
Bourget	Method	ANN – 2 neurons				RF	**PLS-DA**
	$Accuracy_{cal}$	0.995	0.903	0.904	0.906	0.996	**0.969**
	$Accuracy_{pred}$	0.994	0.898	0.899	0.903	0.995	**0.958**
	Qualitative	2	2	2	2	3	**5**
Geneva	Method	ANN – 2 neurons				LDA	**LDA**
	$Accuracy_{cal}$	0.911	0.976	0.976	0.975	0.987	**0.992**
	$Accuracy_{pred}$	0.884	0.979	0.983	0.982	0.989	**0.989**
	Qualitative	1	2	2	2	4	**5**

4.3 Comparison between HSI and naked-eye chronicles

The discretization of the event layers allows for estimation of event layer occurrence along the sediment section and comparison of the event layers with naked-eye event chronicle. The classification map was reduced to a summed profile, with pixels equal to 0 for continuous sedimentation and 1 for an event layer. We assume that the deposits are parallel; if this is not the case, image processing must be used to correct the deformation when possible. This profile can also be used as an event occurrence probability with normalization by the image width in pixels. It was smoothed with a second-order polynomial Savitzky-Golay filter to reduce misclassifications (Savitzky and Golay, 1964). A low threshold (below 20%) allows the separation of all deposits but also the discovery of some artifacts, and the boundaries can be overestimated due to curvatures. Conversely, a high threshold (above 70%) only finds the large deposits, but close ones can be fused. Thus, a double threshold was used. First,

using the half-width of the image to classify each column to one class allowed discovery of the most relevant deposits, but close layers could be observed as a large one. The second threshold of 15% of the image width was used for event layers thicker than 5 mm to potentially divide them. Finally, the chronicle can be reconstructed with the depth and thickness of each event layer. Naked-eye chronicles of the three cores were estimated and can be compared with the hyperspectral ones (Jenny et al., 2014; Rapuc et al., 2020; Wilhelm et al., 2012).

Figure 9 compares the identification of event layers in terms of depth and thickness between the HSI and naked-eye approaches. In general, HSI results in thicker event layers than naked-eye observations. This result can be explained by the limited ability of the eyes to characterize the event limits (resolution grain) or its curvature (misidentification). Machine learning also enables one to identify new deposits that were not visually detected (due to their small thickness or texture or color differences). They must be assessed by other high-resolution techniques such as microscopy to verify their relevance. The number of detected event layers was high (Table 4) due to the detection of supplementary thinner layers.

Initially, this work was developed to study only flood events that were manually labeled. Nonetheless, HSI does not appear to have sufficient discriminant spectral information to distinguish different triggering mechanisms for the event layers (e.g., flood, slumps induced by seismic-shaking, etc.). However, the HSI model is the first fast and non-destructive method to semi-automatically detect event layers in different sedimentary contexts and represents a clear improvement in sedimentology.

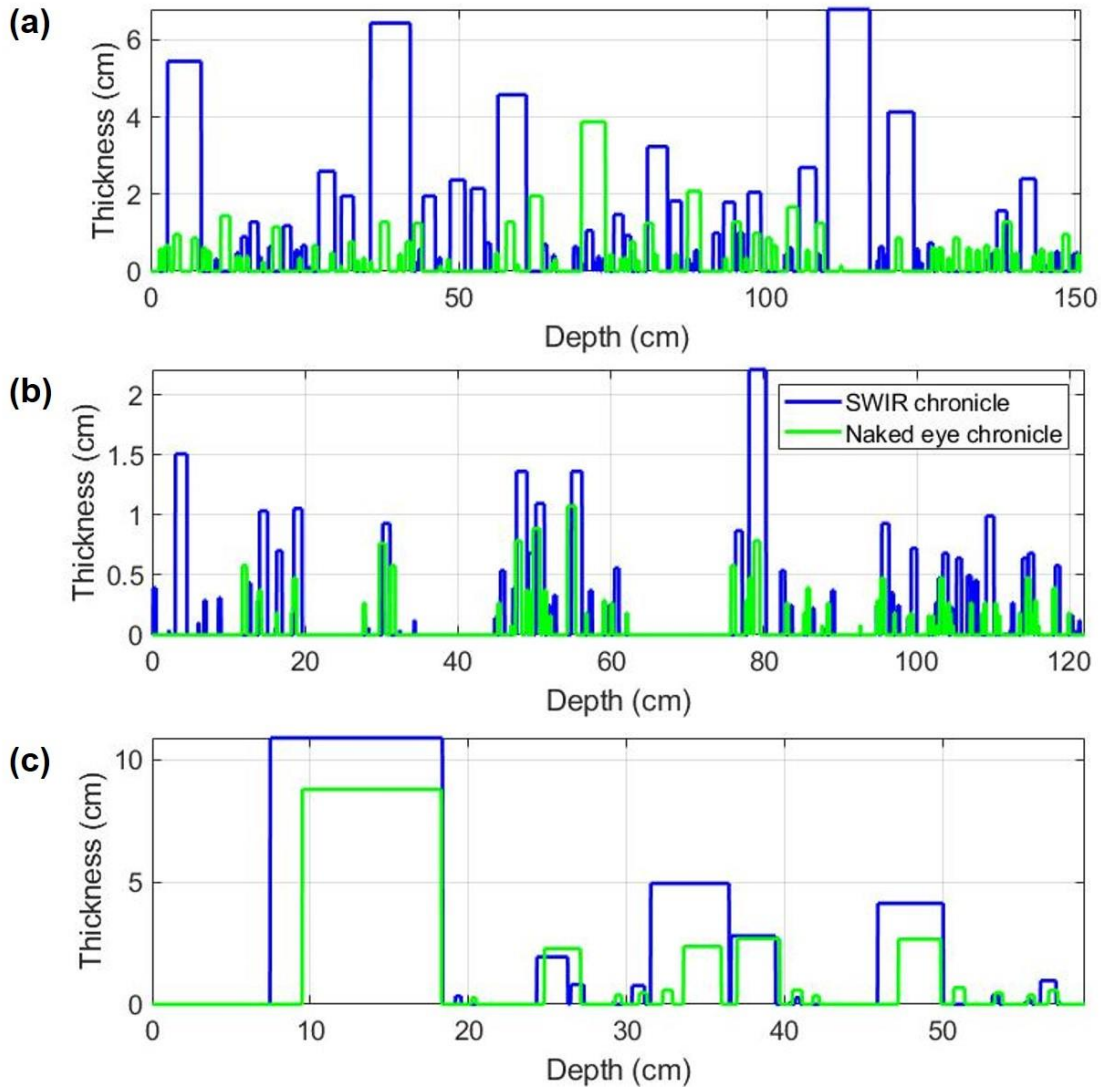

459

460 Figure 9: Comparison of the naked-eye and HSI estimated chronicles for the three samples: (a) Allos; (b) Bourget; (c) Geneva

461 Table 4: Statistics from the naked-eye and HIS event layer detections. N is the number of event layers identified in each lake

462 core, and the other variables are statistics about the layer thickness

		N	$N_{<1\ mm}$	Average (mm)	Standard deviation (mm)	Minimum (mm)	Maximum (mm)
Allos	Naked eye	69	0	7.44	5.73	1.00	39.00
	HSI	88	12	9.64	13.51	0.32	68.19

Bourget	Naked eye	56	0	3.41	2.17	1.00	11.00
	HSI	72	19	4.24	4.28	0.20	22.31
Geneva	Naked eye	15	0	15.93	21.97	3.00	88.00
	his	26	11	11.37	23.81	0.22	109.01

4.4 Perspectives

It is worth noting that we only focused on event layers, and the models are site-specific. Some strategies can be tested in future works. The first strategy would be to create a multi-site database to learn several event types and include continuous sedimentation cases (strata or homogeneous). A second strategy could be to use complementary information estimated by other sensors, such as XRF spectroscopy, which is also a non-destructive high-resolution (up to 200 µm) analysis, for elemental composition (Rapuc et al., 2020).

It would also be interesting to use a spatial-spectral approach to add information contained in both dimensions, such as the color and grain size gradient, along a flood event. Deep learning with a convolutional neural network (CNN) uses this type of approach and could be interesting for a large multi-site database. This method introduces multi-scale local feature learning and some translation and rotation invariance, which are of interest for image classification (Schmidhuber, 2015). We have tested a CNN1D that uses only the spectral dimension, but it has poor performance that may be due to too small of a database and a too simple of a problem that an ANN with few neurons could model. In future work, we will use a CNN3D that uses a spatial-spectral approach (Ben Hamida et al., 2018).

We have shown that the combination of VNIR and SWIR does not increase the discriminating capacity. Improvements can be made with surface defect correction before data acquisition or with pre-processing after data acquisition, or the defects can be detected and removed from the classification map. Another method could be to make two separate classifications with both sensors and

subsequently combine them with different weights using, for example, fuzzy or belief function methods to improve the certainty of the predictions (Lian et al., 2019; Tehrani et al., 2019).

This study has shown that event layers can be estimated at high resolution with hyperspectral imaging in the cores used in the calibration. A first discriminant model based on LDA or PLS-DA, which is estimated with raw hyperspectral data, will enable one to determine the possibility of discrimination among different classes. A similar method has already been used to detect tephra layers (Aymerich et al., 2016). Then, our proposed method may be applied to case studies to detect any type of events such as tsunamis, earthquakes, landslides, storms, and any other laminae. Thus, thanks to a precise manual labeling that includes as much visual and spectral variability as possible, it will be possible to build an automatic log-stratigraphy. This method will be very useful for paleoenvironmental and paleoclimate studies to define the strategy to subsample cores for further analysis to validate predictions or for any other purposes, and it will allow to create event chronicles or to correct the observations from specific events.

5 Conclusions

We studied the potential of three hyperspectral sensors (VNIR, SWIR, VNIR-SWIR) to image three sediment cores and created machine learning models. This study aimed to automatically discriminate different types of sedimentation (continuous versus event layer) with non-destructive, high-resolution, time-saving methods. Six discrimination methods coupled with raw data or eight pre-processing procedures were used to find an optimal model. We found that the SWIR sensor enabled one to create the most robust models with discriminant analysis (LDA, PLS-DA). Raw data presented relevant predictions (0.87-0.95 but qualitative index 2-3), but the use of a pre-processing procedure can slightly improve the performance (0.90—0.98) and robustness (4-5) of the model. The models were quantitatively assessed with prediction accuracies for the three cores of 0.90, 0.95, and 0.98 and qualitative index of 4-5. For the qualitative model, event layers presented colors and textures that differed from those of continuous sedimentation and could be identified with naked-eye observation

to check the relevance of the prediction maps. The discriminant wavelengths are associated with organic matter, some mineral bands, and moisture. This information is not recorded by the VNIR sensor or RGB images, which explains their lower performance, its models seem to rely mainly on the color which is not sufficiently discriminating information. Finally, event chronicles could be estimated from the classification maps by calculating the depth and thickness of each deposit and seem relevant with naked eye chronicles. Unfortunately, the hyperspectral sensors used in this study do not have sufficient spectral discriminant information to characterize the trigger of the event layer and whether different types of events were present in the same sediment core. Future work will enable the characterization of the triggers by combining hyperspectral imaging with other sensors or using spatial-spectral machine learning methods. This study highlights the sediment lithology discrimination capacity of hyperspectral imaging with manual labeling. Future application of this method on sediment sections will allow the creation of robust chronicles of events with characteristic wavelengths and enhance the knowledge about the evolution of the frequency of extreme geodynamic events.

6 Acknowledgements

Coring supports were provided by the French National Research Agency's with the IPER-RETRO program for Lake Geneva (ANR-08-VUL 005) and the Pygmalion project for Lake Allos (ANR BLAN07-2_204489). Hyperspectral imaging was processed at the University of Normandie-Rouen and funded by the Region Normandie, which supports the scientific consortium SCALE UMR CNRS 3730.

7 Computer Code Availability

The Matlab codes used in this study to perform all these processing (machine learning and pre-processing) can be accessed in the following repository:

https://github.com/JacqKevin/HSI_SupervisedClassification.

8 Description of author's responsibilities.

Kévin Jacq: Data acquisition and processing; Algorithm development; Writing original draft

William Rapuc: Data processing; Sedimentology interpretation; Writing original draft

Alexandre Benoit: Machine learning methods; Review and editing the draft

Didier Coquin: Machine learning methods; Review and editing the draft

Bernard Fanget: Spectroscopy and chemometrics methods; Review and editing the draft

Yves Perrette: Spectroscopy and chemometrics methods; Review and editing the draft

Pierre Sabatier: Sedimentology interpretation; Review and editing the draft

Bruno Wilhelm: Flood event interpretation; Data processing; Review and editing the draft

Maxime Debret: Data acquisition; Review and editing the draft

Fabien Arnaud: Data processing; Review and editing the draft

8 References

Arnaud, F., 2005. Discriminating Bio-Induced and Detrital Sedimentary Processes from Particle Size Distribution of Carbonates and Non-Carbonates in Hard Water Lake Sediments. J. Paleolimnol. 34, 519–526. https://doi.org/10.1007/s10933-005-6787-1

Aymerich, I.F., Oliva, M., Giralt, S., Martín-Herrero, J., 2016. Detection of tephra layers in Antarctic sediment cores with hyperspectral imaging. PLoS One 11, 1–24. https://doi.org/10.1371/journal.pone.0146578

Barnes, R.J., Dhanoa, M.S., Lister, S.J., 1989. Standard Normal Variate Transformation and De-Trending of Near-Infrared Diffuse Reflectance Spectra. Appl. Spectrosc. 43, 772–777. https://doi.org/10.1366/0003702894202201

Ben Hamida, A., Benoit, A., Lambert, P., Ben Amar, C., 2018. 3-D Deep Learning Approach for Remote Sensing Image Classification. IEEE Trans. Geosci. Remote Sens. 56, 4420–4434. https://doi.org/10.1109/TGRS.2018.2818945

Bora, D.J., Gupta, A.K., Khan, F.A., 2015. Comparing the performance of L*A*B* and HSV color spaces with respect to color image segmentation. Int. J. Emerg. Technol. Adv. Eng. 5, 192–203.

Breiman, L., Friedman, J.H., Olshen, R.A., Stone, C.J., 1984. Classification And Regression Trees. Routledge. https://doi.org/10.1201/9781315139470

Bull, C.R., 1991. Wavelength selection for near-infrared reflectance moisture meters. J. Agric. Eng. Res. 49, 113–125. https://doi.org/10.1016/0021-8634(91)80032-A

Butz, C., Grosjean, M., Fischer, D., Wunderle, S., Tylmann, W., Rein, B., 2015. Hyperspectral imaging spectroscopy: a promising method for the biogeochemical analysis of lake sediments. J. Appl. Remote Sens. 9, 1–20. https://doi.org/10.1117/1.JRS.9.096031

Butz, C., Grosjean, M., Goslar, T., Tylmann, W., 2017. Hyperspectral imaging of sedimentary bacterial

563 pigments: a 1700-year history of meromixis from varved Lake Jaczno, northeast Poland. J.
564 Paleolimnol. 1–16. https://doi.org/10.1007/s10933-017-9955-1

565 Chabrillat, S., Milewski, R., Schmid, T., Rodriguez, M., Escribano, P., Pelayo, M., Palacios-Orueta, A.,
566 2014. Potential of hyperspectral imagery for the spatial assessment of soil erosion stages in
567 agricultural semi-arid Spain at different scales, in: International Geoscience and Remote Sensing
568 Symposium (IGARSS). Institute of Electrical and Electronics Engineers Inc., pp. 2918–2921.
569 https://doi.org/10.1109/IGARSS.2014.6947087

570 Chagué-Goff, C., 2010. Chemical signatures of palaeotsunamis: A forgotten proxy? Mar. Geol. 271,
571 67–71. https://doi.org/10.1016/j.margeo.2010.01.010

572 CIE, 1999. IEC 61966-2-1:1999: Multimedia systems and equipment - Colour measurement and
573 management - Part 2-1: Colour management - Default RGB colour space - sRGB.

574 Cloutis, E.A., 1989. Spectral reflectance properties of hydrocarbons: Remote-sensing implications.
575 Science (80-.). 245, 165–168. https://doi.org/10.1126/science.245.4914.165

576 Contreras Acosta, I.C., Khodadadzadeh, M., Tolosana Delgado, R., Gloaguen, R., 2020. Drill-core
577 hyperspectral and geochemical data integration in a superpixel-based machine learning
578 framework. IEEE J. Sel. Top. Appl. Earth Obs. Remote Sens. 1–16.
579 https://doi.org/10.1109/JSTARS.2020.3011221

580 Contreras Acosta, I.C., Khodadadzadeh, M., Tusa, L., Ghamisi, P., Gloaguen, R., 2019. A Machine
581 learning framework for drill-core mineral mapping using hyperspectral and high-resolution
582 mineralogical data fusion. IEEE J. Sel. Top. Appl. Earth Obs. Remote Sens. 12.
583 https://doi.org/10.1109/JSTARS.2019.2924292

584 Dumke, I., Nornes, S.M., Purser, A., Marcon, Y., Ludvigsen, M., Ellefmo, S.L., Johnsen, G., Søreide, F.,
585 2018. First hyperspectral imaging survey of the deep seafloor: High-resolution mapping of
586 manganese nodules. Remote Sens. Environ. 209, 19–30.

https://doi.org/10.1016/j.rse.2018.02.024

Ebert, T., Trauth, M.H., 2015. Semi-automated detection of annual laminae (varves) in lake sediments using a fuzzy logic algorithm. Palaeogeogr. Palaeoclimatol. Palaeoecol. 435, 272–282. https://doi.org/10.1016/j.palaeo.2015.05.024

Feng, J., Rogge, D., Rivard, B., 2018. Comparison of lithological mapping results from airborne hyperspectral VNIR-SWIR, LWIR and combined data. Int. J. Appl. Earth Obs. Geoinf. 64, 340–353. https://doi.org/10.1016/J.JAG.2017.03.003

Feng, W., Qi, S., Heng, Y., Zhou, Y., Wu, Y., Liu, W., He, L., Li, X., 2017. Canopy vegetation indices from in situ hyperspectral data to assess plant water status of winter wheat under powdery mildew stress. Front. Plant Sci. 8. https://doi.org/10.3389/fpls.2017.01219

Fisher, R.A., 1936. The Use of Multiple Measurements in Taxonomic Problems. Ann. Eugen. 7, 179–188. https://doi.org/10.1111/j.1469-1809.1936.tb02137.x

Fouinat, L., Sabatier, P., Poulenard, J., Reyss, J.-L., Montet, X., Arnaud, F., 2017. A new CT scan methodology to characterize a small aggregation gravel clast contained in a soft sediment matrix. Earth Surf. Dyn. 5, 199–209. https://doi.org/10.5194/esurf-5-199-2017

Gaume, E., Bain, V., Bernardara, P., Newinger, O., Barbuc, M., Bateman, A., Blaškovičová, L., Blöschl, G., Borga, M., Dumitrescu, A., Daliakopoulos, I., Garcia, J., Irimescu, A., Kohnova, S., Koutroulis, A., Marchi, L., Matreata, S., Medina, V., Preciso, E., Sempere-Torres, D., Stancalie, G., Szolgay, J., Tsanis, I., Velasco, D., Viglione, A., 2009. A compilation of data on European flash floods. J. Hydrol. 367, 70–78. https://doi.org/10.1016/J.JHYDROL.2008.12.028

Ghamisi, P., Plaza, J., Chen, Y., Li, J., Plaza, A.J., 2017. Advanced Spectral Classifiers for Hyperspectral Images: A review. IEEE Geosci. Remote Sens. Mag. 5, 8–32. https://doi.org/10.1109/MGRS.2016.2616418

Giguet-Covex, C., Arnaud, F., Poulenard, J., Enters, D., Reyss, J.-L., Millet, L., Lazzaroto, J., Vidal, O.,

2010. Sedimentological and geochemical records of past trophic state and hypolimnetic anoxia in large, hard-water Lake Bourget, French Alps. J. Paleolimnol. 43, 171–190. https://doi.org/10.1007/s10933-009-9324-9

Gilli, A., Anselmetti, F.S., Glur, L., Wirth, S.B., 2013. Lake Sediments as Archives of Recurrence Rates and Intensities of Past Flood Events, in: Dating Torrential Processes on Fans and Cones: Methods and Their Application for Hazard and Risk Assessment. pp. 225–242. https://doi.org/10.1007/978-94-007-4336-6_15

Glur, L., Wirth, S.B., Büntgen, U., Gilli, A., Haug, G.H., Schär, C., Beer, J., Anselmetti, F.S., 2013. Frequent floods in the European Alps coincide with cooler periods of the past 2500 years. Sci. Rep. 3, 2770. https://doi.org/10.1038/srep02770

Hernández-Hernández, J.L., García-Mateos, G., González-Esquiva, J.M., Escarabajal-Henarejos, D., Ruiz-Canales, A., Molina-Martínez, J.M., 2016. Optimal color space selection method for plant/soil segmentation in agriculture. Comput. Electron. Agric. 122, 124–132. https://doi.org/10.1016/J.COMPAG.2016.01.020

Ho, T.K., 1995. Random decision forests, in: Proceedings of 3rd International Conference on Document Analysis and Recognition. IEEE Comput. Soc. Press, pp. 278–282. https://doi.org/10.1109/ICDAR.1995.598994

Ivakhnenko, A., Lapa, V.G., 1965. Cybernetic predicting devices. CCM Information Corp., New York.

Jacq, K., Coquin, D., Fanget, B., Perrette, Y., Debret, M., 2019a. Study of pansharpening methods applied to hyperspectral images of sediment cores, in: 2019 22nd International Conference on Information Fusion (FUSION). Ottawa, Canada, pp. 1–6.

Jacq, K., Giguet-Covex, C., Sabatier, P., Perrette, Y., Fanget, B., Coquin, D., Debret, M., Arnaud, F., 2019b. High-resolution grain size distribution of sediment core with hyperspectral imaging. Sediment. Geol. 393–394. https://doi.org/10.1016/j.sedgeo.2019.105536

635 Jacq, K., Martinez-Lamas, R., Van Exem, A., Debret, M., 2020. Hyperspectral core-logger image
636 acquisition, Protocols.io.

637 Jacq, K., Perrette, Y., Fanget, B., Sabatier, P., Coquin, D., Martinez-Lamas, R., Debret, M., Arnaud, F.,
638 2019c. High-resolution prediction of organic matter concentration with hyperspectral imaging
639 on a sediment core. Sci. Total Environ. 663, 236–244.
640 https://doi.org/10.1016/j.scitotenv.2019.01.320

641 Jenny, J.-P., 2013. Réponses des grands lacs périalpins aux pressions anthropiques et climatiques
642 récentes : reconstitutions spatio-temporelles à partir d'archives sédimentaires. HAL. Université
643 Grenoble Alpes.

644 Jenny, J.-P., Wilhelm, B., Arnaud, F., Sabatier, P., Giguet Covex, C., Mélo, A., Fanget, B., Malet, E.,
645 Ployon, E., Perga, M.E., 2014. A 4D sedimentological approach to reconstructing the flood
646 frequency and intensity of the Rhône River (Lake Bourget, NW European Alps). J. Paleolimnol.
647 51, 469–483. https://doi.org/10.1007/s10933-014-9768-4

648 Khaledian, Y., Miller, B.A., 2020. Selecting appropriate machine learning methods for digital soil
649 mapping. Appl. Math. Model. 81, 401–418. https://doi.org/10.1016/j.apm.2019.12.016

650 Krupnik, D., Khan, S., 2019. Close-range, ground-based hyperspectral imaging for mining applications
651 at various scales: Review and case studies. Earth-Science Rev. 198, 34.
652 https://doi.org/10.1016/j.earscirev.2019.102952

653 Li, S., Song, W., Fang, L., Chen, Y., Ghamisi, P., Benediktsson, J.A., 2019. Deep learning for
654 hyperspectral image classification: An overview. IEEE Trans. Geosci. Remote Sens. 57.
655 https://doi.org/10.1109/TGRS.2019.2907932

656 Lian, C., Ruan, S., Denoeux, T., Li, H., Vera, P., 2019. Joint Tumor Segmentation in PET-CT Images
657 Using Co-Clustering and Fusion Based on Belief Functions. IEEE Trans. Image Process. 28, 755–
658 766. https://doi.org/10.1109/TIP.2018.2872908

659 Liu, C., Yuen, J., Torralba, A., 2011. SIFT flow: dense correspondence across scenes and its
660 applications. IEEE Trans. Pattern Anal. Mach. Intell. 33, 978–994.
661 https://doi.org/10.1109/TPAMI.2010.147

662 Lorenz, S., Seidel, P., Ghamisi, P., Zimmermann, R., Tusa, L., Khodadadzadeh, M., Contreras, I.C.,
663 Gloaguen, R., 2019. Multi-Sensor Spectral Imaging of Geological Samples: A Data Fusion
664 Approach Using Spatio-Spectral Feature Extraction. Sensors 19, 2787.
665 https://doi.org/10.3390/s19122787

666 Lotter, andré f., Lemcke, G., 1999. Methods for preparing and counting biochemical varves. Boreas
667 28, 243–252. https://doi.org/10.1111/j.1502-3885.1999.tb00218.x

668 Makri, S., Rey, F., Gobet, E., Gilli, A., Tinner, W., Grosjean, M., 2020. Early human impact in a 15,000-
669 year high-resolution hyperspectral imaging record of paleoproduction and anoxia from a varved
670 lake in Switzerland. Quat. Sci. Rev. 239, 1–14. https://doi.org/10.1016/j.quascirev.2020.106335

671 McCulloch, W.S., Pitts, W., 1943. A logical calculus of the ideas immanent in nervous activity. Bull.
672 Math. Biophys. 5, 115–133. https://doi.org/10.1007/BF02478259

673 Meyer, M.C., Faber, R., Spö Tl, C., 2006. The WinGeol Lamination Tool : new software for rapid, semi
674 - automated analysis of laminated climate archives. The Holocene 16, 753–761.
675 https://doi.org/10.1191/0959683606hl969rr

676 Ndiaye, M., Davaud, E., Ariztegui, D., Fall, M., 2012. A semi automated method for laminated
677 sediments analysis. Int. J. Geosci. 3, 206–210. https://doi.org/10.4236/ijg.2012.31023

678 Pearson, K., 1901. On lines and planes of closest fit to systems of points in space. Philos. Mag. 2, 559–
679 572. https://doi.org/10.1080/14786440109462720

680 Peerbhay, K.Y., Mutanga, O., Ismail, R., 2015. Random Forests Unsupervised Classification: The
681 Detection and Mapping of Solanum mauritianum Infestations in Plantation Forestry Using
682 Hyperspectral Data. IEEE J. Sel. Top. Appl. Earth Obs. Remote Sens. 8, 3107–3122.

https://doi.org/10.1109/JSTARS.2015.2396577

Rapuc, W., Jacq, K., Develle, A.-L., Sabatier, P., Fanget, B., Perrette, Y., Coquin, D., Debret, M., Wilhelm, B., Arnaud, F., 2020. XRF and hyperspectral analyses as an automatic way to detect flood events in sediment cores. Sediment. Geol. 409, 1–10. https://doi.org/10.1016/j.sedgeo.2020.105776

Rinnan, Å., Berg, F. van den, Engelsen, S.B., 2009. Review of the most common pre-processing techniques for near-infrared spectra. TrAC Trends Anal. Chem. 28, 1201–1222. https://doi.org/10.1016/J.TRAC.2009.07.007

Rosenblatt, F., 1958. The Perceptron: A Probabilistic Model for Information Storage and Organization in The Brain. Psychol. Rev. 65, 386–408.

Rubwurm, M., Korner, M., 2017. Temporal Vegetation Modelling Using Long Short-Term Memory Networks for Crop Identification from Medium-Resolution Multi-spectral Satellite Images, in: IEEE Computer Society Conference on Computer Vision and Pattern Recognition Workshops. IEEE Computer Society, pp. 1496–1504. https://doi.org/10.1109/CVPRW.2017.193

Sabatier, P., Dezileau, L., Colin, C., Briqueu, L., Bouchette, F., Martinez, P., Siani, G., Raynal, O., Von Grafenstein, U., 2012. 7000 years of paleostorm activity in the NW Mediterranean Sea in response to Holocene climate events. Quat. Res. 77, 1–11. https://doi.org/10.1016/j.yqres.2011.09.002

Savitzky, A., Golay, M.J.E., 1964. Smoothing and Differentiation of Data by Simplified Least Squares Procedures. Anal. Chem. 36, 1627–1639. https://doi.org/10.1021/ac60214a047

Schmidhuber, J., 2015. Deep Learning in Neural Networks: An Overview. Neural Networks 61, 85–117. https://doi.org/10.1016/j.neunet.2014.09.003

Schneider, T., Rimer, D., Butz, C., Grosjean, M., 2018. A high-resolution pigment and productivity record from the varved Ponte Tresa basin (Lake Lugano, Switzerland) since 1919: insight from

an approach that combines hyperspectral imaging and high-performance liquid chromatography. J. Paleolimnol. 1–18. https://doi.org/10.1007/s10933-018-0028-x

Shang, X., Chisholm, L.A., 2014. Classification of Australian native forest species using hyperspectral remote sensing and machine-learning classification algorithms. IEEE J. Sel. Top. Appl. Earth Obs. Remote Sens. 7, 2481–2489. https://doi.org/10.1109/JSTARS.2013.2282166

Shi, C., Wang, L., 2014. Incorporating spatial information in spectral unmixing: A review. Remote Sens. Environ. 149, 70–87. https://doi.org/10.1016/j.rse.2014.03.034

Tehrani, A.K.N., Macktoobian, M., Kasaei, S., 2019. Color Image Segmentation Using a Fuzzy Inference System, in: Proceedings - 2019 7th International Conference on Digital Information Processing and Communications, ICDIPC 2019. Institute of Electrical and Electronics Engineers Inc., pp. 78–83. https://doi.org/10.1109/ICDIPC.2019.8723780

Teke, M., Deveci, H.S., Haliloglu, O., Gurbuz, S.Z., Sakarya, U., 2013. A short survey of hyperspectral remote sensing applications in agriculture, in: RAST 2013 - Proceedings of 6th International Conference on Recent Advances in Space Technologies. pp. 171–176. https://doi.org/10.1109/RAST.2013.6581194

Tusa, L., Andreani, L., Khodadadzadeh, M., Contreras, C., Ivascanu, P., Gloaguen, R., Gutzmer, J., 2019. Mineral mapping and vein detection in hyperspectral drill-core scans: Application to porphyry-type mineralization. Minerals 9. https://doi.org/10.3390/min9020122

Tusa, L., Kern, M., Khodadadzadeh, M., Blannin, R., Gloaguen, R., Gutzmer, J., 2020a. Evaluating the performance of hyperspectral short-wave infrared sensors for the pre-sorting of complex ores using machine learning methods. Miner. Eng. 146, 106150. https://doi.org/10.1016/j.mineng.2019.106150

Tusa, L., Khodadadzadeh, M., Contreras, C., Shahi, K.R., Fuchs, M., Gloaguen, R., Gutzmer, J., 2020b. Drill-Core Mineral Abundance Estimation Using Hyperspectral and High-Resolution

731 Mineralogical Data. Remote Sens. 12. https://doi.org/10.3390/rs12071218

732 Van Exem, A., 2018. Reconstructions de changements environnementaux dans les archives lacustres
733 par imagerie hyperspectrale. HAL. Université de Rouen Normandie.

734 Vannière, B., Magny, M., Joannin, S., Simonneau, A., Wirth, S.B., Hamann, Y., Chapron, E., Gilli, A.,
735 Desmet, M., Anselmetti, F.S., 2013. Orbital changes, variation in solar activity and increased
736 anthropogenic activities: controls on the Holocene flood frequency in the Lake Ledro area,
737 Northern Italy. Clim. Past 9, 1193–1209. https://doi.org/10.5194/cp-9-1193-2013

738 Verpoorter, C., Carrère, V., Combe, J.-P., 2014. Visible, near-infrared spectrometry for simultaneous
739 assessment of geophysical sediment properties (water and grain size) using the Spectral
740 Derivative-Modified Gaussian Model. J. Geophys. Res. Earth Surf. 119, 2098–2122.
741 https://doi.org/10.1002/2013JF002969

742 Vidal, M., Amigo, J.M., 2012. Pre-processing of hyperspectral images. Essential steps before image
743 analysis. Chemom. Intell. Lab. Syst. 117, 138–148.
744 https://doi.org/10.1016/j.chemolab.2012.05.009

745 Viscarra Rossel, R.A., Behrens, T., 2010. Using data mining to model and interpret soil diffuse
746 reflectance spectra. Geoderma 158, 46–54. https://doi.org/10.1016/j.geoderma.2009.12.025

747 Weber, M.E., Reichelt, L., Kuhn, G., Pfeiffer, M., Korff, B., Thurow, J., Ricken, W., 2010. BMPix and
748 PEAK tools: new methods for automated laminae recognition and counting-application to
749 glacial varves from Antarctic marine sediment. Geochemistry, Geophys. Geosystems 11.
750 https://doi.org/10.1029/2009GC002611

751 Wilhelm, B., Arnaud, F., Sabatier, P., Crouzet, C., Brisset, E., Chaumillon, E., Disnar, J.-R., Guiter, F.,
752 Malet, E., Reyss, J.-L., Tachikawa, K., Bard, E., Delannoy, J.-J., 2012. 1400 years of extreme
753 precipitation patterns over the Mediterranean French Alps and possible forcing mechanisms.
754 Quat. Res. 78, 1–12. https://doi.org/10.1016/J.YQRES.2012.03.003

Wilhelm, B., Ballesteros Canovas, J.A., Corella Aznar, J.P., Kämpf, L., Swierczynski, T., Stoffel, M., Støren, E., Toonen, W., 2018. Recent advances in paleoflood hydrology: From new archives to data compilation and analysis. Water Secur. 3, 1–8. https://doi.org/10.1016/j.wasec.2018.07.001

Wilhelm, B., Nomade, J., Crouzet, C., Litty, C., Sabatier, P., Belle, S., Rolland, Y., Revel, M., Courboulex, F., Arnaud, F., Anselmetti, F.S., 2016. Quantified sensitivity of small lake sediments to record historic earthquakes: Implications for paleoseismology. J. Geophys. Res. Earth Surf. 121, 2–16. https://doi.org/10.1002/2015JF003644

Wilhelm, B., Sabatier, P., Arnaud, F., 2015. Is a regional flood signal reproducible from lake sediments? Sedimentology 62, 1103–1117. https://doi.org/10.1111/sed.12180

Wold, S., Ruhe, A., Wold, H., Dunn, III, W.J., 1984. The Collinearity Problem in Linear Regression. The Partial Least Squares (PLS) Approach to Generalized Inverses. SIAM J. Sci. Stat. Comput. 5, 735–743. https://doi.org/10.1137/0905052

Zuiderveld, K., 1994. Contrast Limited Adaptive Histogram Equalization, in: Graphics Gems IV. Academic Press, pp. 474–485. https://doi.org/10.1016/B978-0-12-336156-1.50061-6

9 List of captions

9.1 Figures

Figure 1: Locations, tributaries and effluents of the lakes: (a) Bourget and Geneva, (b) Allos.

Figure 2: XRF analysis for Ti, Zr/K, and Ca of the three cores: (a) Allos, (b) Bourget, and (c) Geneva

Figure 3: Data processing to create a classification model to predict each pixel: (1) Visualization with RGB images at both resolutions; (2) Manual labeling of the image; (3) Data pre-processing and (4) Creation of supervised classification models for each dataset (DT: Decision Tree, RF: Random Forest, ANN: Artificial Neural Network, LDA: Linear Discriminant Analysis, QDA: Quadratic Discriminant Analysis, PLS-DA: Partial Least Squares Discriminant Analysis); (5) Prediction for each image; (6) Estimation of the optimal model depending on the sensor, pre-processing procedure and discrimination model

Figure 4: Spectral variations of labelled pixels for each class (blue = event layers; yellow = continuous sedimentation) and for the three cores: (a) Allos, (b) Bourget and (c) Geneva. The reflectance of the sediments depends on the specific sedimentary properties of the sites studied. It seems difficult to visually estimate specific discriminating spectral areas of the two classes studied

Figure 5: Schematic representation of the machine learning methods used in this study depending on their basis: (a) rules; (b) neurons; and (c) functions

Figure 6: Radar charts of the impact of pre-processing on the overall prediction accuracy of each classification method and lake core hyperspectral image (a-c: Lake Allos; d-f: Lake Bourget; g-i: Lake Geneva; a, d, g: VNIR sensor; b, e, h: SWIR sensor; c, f, i: VNIR-SWIR sensor)

Figure 7: Optimal (c, f, i) and worst (b, e, h) models for each sediment core sample (a, b, c: Allos; d, e, f: Bourget; h, i, j: Geneva) and labeled areas (blue = event layers; yellow = continuous sedimentation)

Figure 8: Comparison of the normalized coefficients (coefficient weights normalized to one for each method) used by the optimal SWIR models to highlight the discriminant wavelengths: (a) Allos, (b) Bourget, and (c) Geneva samples

Figure 9: Comparison of the naked-eye and HSI estimated chronicles for the three samples: (a) Allos; (b) Bourget; (c) Geneva

9.2 Tables

Table 1: Optimal models for each sensor depending on the sample and discrimination method and based on the parameters indicating their performance and rubustness

Table 2: Comparison of site-specific models for the generalization to the other cores

Table 3: Comparison of the conventional image discriminant models with the optimal predictions being estimated by the hyperspectral images

Table 4: Statistics from the naked-eye and HSI event layer detections. N is the number of event layers identified in each lake core, and the other variables are statistics about the layer thickness

10 Supplementary Material

10.1 Figures

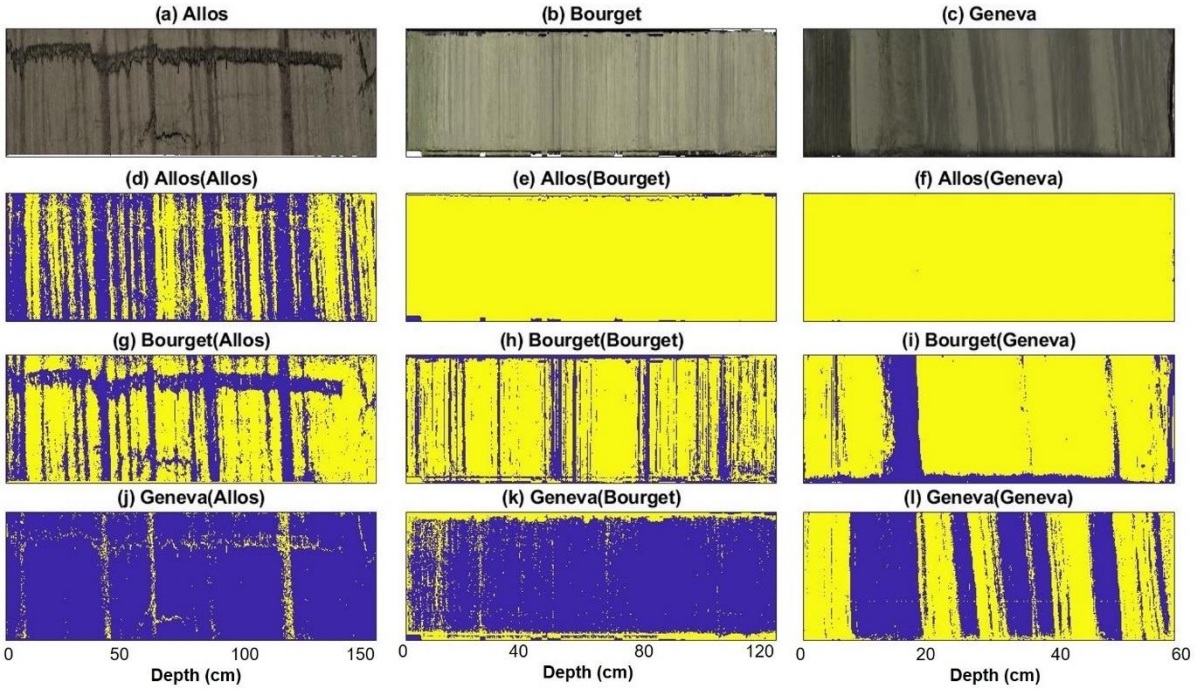

Supplementary figure 1: Classification maps estimated by model re-using: (d-e-f): Allos model; (g-h-i): Bourget model; (j-k-l): Geneva model; (d-g-j): Allos data; (e-h-k): Bourget data; (f-i-l): Geneva data.

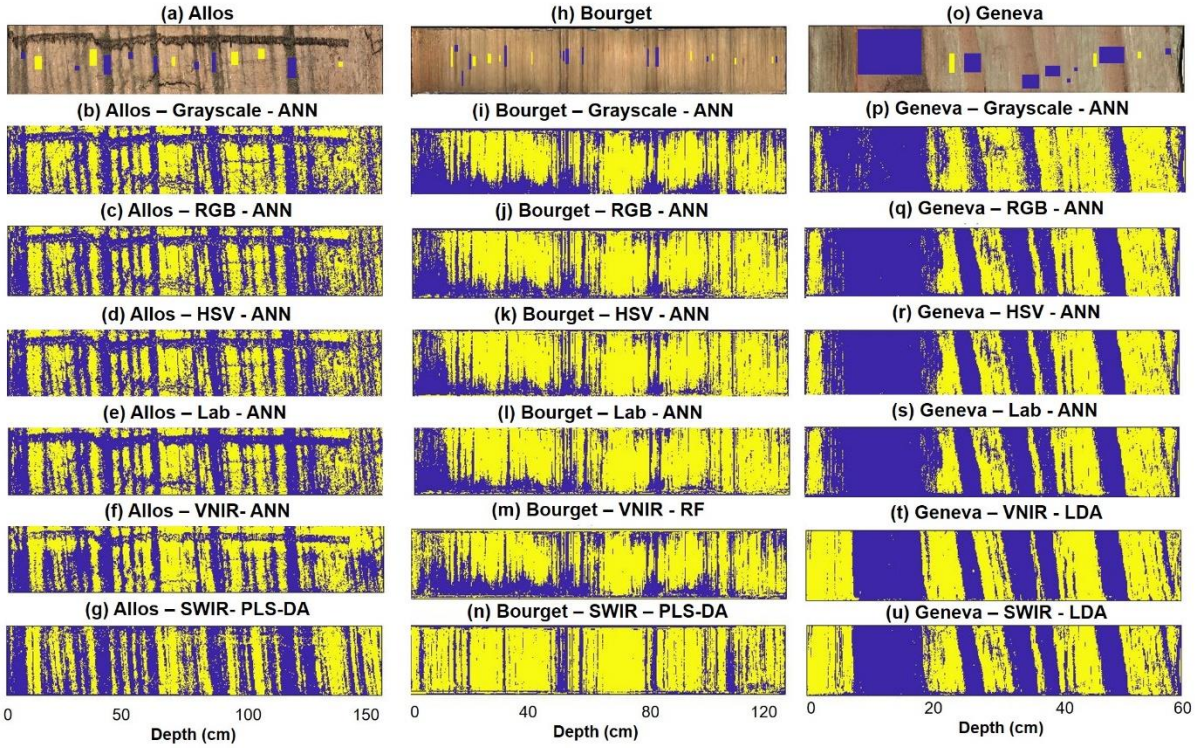

Supplementary figure 2: Comparison of the classification maps estimated by the learning of the conventional images and HSI

10.2 Tables

Supplementary table 1: Parameters of each machine learning method

Method	Parameters
DT	Split predictor: Standard CART Split criterion: Gini's diversity index Decision tree pruning based on error criterion
RF	Ensemble-aggregation method: Adaptive logistic regression Number of ensemble learning cycles: 100
ANN	Number of neurons: 2-10 Training function: Scaled conjugate gradient backpropagation Performance function: Cross-Entropy

LDA	Discriminant type: Linear
QDA	Discriminant type: Quadratic
PLS-DA	Latent variable estimation method: NIPALS Maximum number of latent variables: 15 Selection of the number of latent variables: R^2 differences between two consecutive latent variables are less than 2%

817

818 Supplementary table 2: The number of pixels for each sediment core image and the number of labeled pixels for the

819 calibration and validation sets for each class (1=event layer; 2=continuous sedimentation)

Sample	Sensors	Total pixels	Class	Number of areas labeled and pixels	Calibration pixels	Validation pixels
Allos	VNIR	30 433 152	1	8 areas, 598 722 (1.97%)	419 105 (1.38%)	179 617 (0.59%)
			2	6 areas, 961 079 (3.16%)	419 105 (1.38%)	541 974 (1.78%)
	SWIR, VNIR-SWIR	1 702 476	1	8 areas, 35 364 (2.08%)	24 755 (1.45%)	10 609 (0.62%)
			2	8 areas, 56 261 (3.30%)	24 755 (1.45%)	31 506 (1.85%)
Bourget	VNIR	21 096 723	1	12 areas, 155 876 (0.74%)	68 636 (0.33%)	87 240 (0.41%)
			2	9 areas, 98 051 (0.46%)	68 636 (0.33%)	29 415 (0.14%)
	SWIR, VNIR-SWIR	1 806 624	1	12 areas, 12 975 (0.72%)	5 709 (0.32%)	7 266 (0.40%)

			2	9 areas, 8 156 (0.45%)	5 709 (0.32%)	2 447 (0.14%)
Geneva	VNIR	13 711 712	1	8 areas, 2 034 596 (14.84%)	65 769 (0.48%)	1 968 827 (14.36%)
			2	3 areas, 93 956 (0.69%)	65 769 (0.48%)	28 187 (0.21%)
	SWIR, VNIR-SWIR	865 234	1	8 areas, 135 933 (15.71%)	4 078 (0.47%)	131 855 (15.24%)
			2	3 areas, 5 826 (0.67%)	4 078 (0.47%)	1 748 (0.20%)

820 Supplementary table 3: Optimal models for the VNIR data depending on the sample and discrimination method

Sample	Performances	DT	RF	ANN	LDA	QDA	PLS-DA
Allos	Processing	CLAHE	Detrend	CLAHE	CLAHE	CLAHE	CLAHE
	Neurons			2			
	$Accuracy_{cal}$	0.978	0.886	0.889	0.863	0.860	0.840
	$Precision_{cal}$	0.977	0.883	0.889	0.904	0.906	0.902
	$Recall_{cal}$	0.980	0.890	0.888	0.811	0.803	0.762
	$Accuracy_{pred}$	0.828	0.882	0.890	0.889	0.889	0.879
	$Precision_{pred}$	0.614	0.710	0.728	0.759	0.764	0.755
	$Recall_{pred}$	0.834	0.888	0.889	0.812	0.804	0.763
	Qualitative	3	3	3	2	2	2

	Computation time (s)	42.544	1272.513	263.840	8.086	251.592	12.975
Bourget	Processing	Raw	Raw	Raw	Raw	Raw	Raw
	Neurons			2			
	$Accuracy_{cal}$	0.999	0.996	0.996	0.994	0.994	0.993
	$Precision_{cal}$	0.999	0.996	0.996	0.998	0.997	0.997
	$Recall_{cal}$	0.999	0.996	0.996	0.990	0.991	0.988
	$Accuracy_{pred}$	0.994	0.995	0.996	0.993	0.992	0.991
	$Precision_{pred}$	0.998	0.998	0.998	0.999	0.999	0.999
	$Recall_{pred}$	0.993	0.995	0.996	0.991	0.991	0.988
	Qualitative	2	3	2	2	2	2
	Computation time (s)	1.817	139.542	5.174	1.216	54.210	2.057
Geneva	Processing	Detrend	Detrend	Detrend	Detrend	Detrend	Detrend
	Neurons			2			
	$Accuracy_{cal}$	0.998	0.990	0.992	0.987	0.987	0.985
	$Precision_{cal}$	0.998	0.985	0.989	0.985	0.985	0.984
	$Recall_{cal}$	0.999	0.995	0.994	0.988	0.988	0.985
	$Accuracy_{pred}$	0.987	0.993	0.994	0.989	0.989	0.985
	$Precision_{pred}$	1.000	1.000	1.000	1.000	1.000	1.000
	$Recall_{pred}$	0.987	0.993	0.994	0.989	0.989	0.986

	Qualitative	2	2	2	3	3	3
	Computation time (s)	2.615	200.019	16.167	1.142	52.417	2.814

821 Supplementary table 4: Optimal models for the SWIR data depending on the sample and discrimination method

Sample	Performances	DT	RF	ANN	LDA	QDA	PLS-DA
Allos	Processing	Raw	SNV	Autoscale	Raw	Raw	SNV
	Neurons			3			
	$Accuracy_{cal}$	0.982	0.925	0.922	0.920	0.920	0.900
	$Precision_{cal}$	0.982	0.949	0.944	0.933	0.933	0.908
	$Recall_{cal}$	0.982	0.898	0.896	0.905	0.904	0.890
	$Accuracy_{pred}$	0.876	0.928	0.935	0.927	0.926	0.902
	$Precision_{pred}$	0.725	0.853	0.869	0.840	0.840	0.785
	$Recall_{pred}$	0.882	0.888	0.895	0.904	0.903	0.885
	Qualitative	3	5	5	5	5	5
	Computation time (s)	1.214	95.740	6.989	0.664	39.287	0.800
Bourget	Processing	Detrend	Detrend	Detrend	Detrend	Detrend	Detrend
	Neurons			2			
	$Accuracy_{cal}$	0.994	1.000	0.976	0.971	0.972	0.969
	$Precision_{cal}$	0.995	1.000	0.994	0.993	0.994	0.988
	$Recall_{cal}$	0.993	1.000	0.958	0.949	0.949	0.951

	$Accuracy_{pred}$	0.952	0.959	0.967	0.954	0.955	0.958
	$Precision_{pred}$	0.984	0.986	0.997	0.997	0.997	0.996
	$Recall_{pred}$	0.953	0.961	0.960	0.944	0.944	0.949
	Qualitative	2	3	4	5	5	5
	Computation time (s)	0.266	10.402	0.402	0.167	24.268	0.219
Geneva	Processing	SNV	SNV	SNV	SNV	SNV	SNV
	Neurons			2			
	$Accuracy_{cal}$	0.998	1.000	0.996	0.992	0.992	0.991
	$Precision_{cal}$	0.998	1.000	0.998	0.996	0.996	0.996
	$Recall_{cal}$	0.999	1.000	0.994	0.989	0.988	0.985
	$Accuracy_{pred}$	0.991	0.993	0.993	0.989	0.988	0.987
	$Precision_{pred}$	1.000	1.000	1.000	1.000	1.000	1.000
	$Recall_{pred}$	0.991	0.993	0.993	0.989	0.988	0.987
	Qualitative	3	4	4	5	5	5
	Computation time (s)	0.155	5.436	0.255	0.113	21.478	0.163

822 Supplementary table 5: Optimal models for the VNIR-SWIR data depending on the sample and discrimination method

Sample	Performances	DT	RF	ANN	LDA	QDA	PLS-DA
Allos	Processing	CLAHE	SNV	SNV	Raw	Raw	SNV
	Neurons			2			

	$Accuracy_{cal}$	0.984	0.943	0.933	0.931	0.931	0.901
	$Precision_{cal}$	0.983	0.961	0.952	0.940	0.940	0.943
	$Recall_{cal}$	0.984	0.924	0.912	0.921	0.921	0.855
	$Accuracy_{pred}$	0.877	0.931	0.940	0.935	0.935	0.921
	$Precision_{pred}$	0.726	0.854	0.875	0.856	0.856	0.857
	$Recall_{pred}$	0.886	0.899	0.911	0.918	0.918	0.855
	Qualitative	3	5	4	5	5	5
	Computation time (s)	2.726	86.900	15.562	1.097	49.604	1.206
Bourget	Processing	Raw	Raw	Raw	Detrend	Detrend	Raw
	Neurons			2			
	$Accuracy_{cal}$	0.993	1.000	0.981	0.979	0.979	0.979
	$Precision_{cal}$	0.995	0.999	0.998	0.997	0.997	0.997
	$Recall_{cal}$	0.992	1.000	0.963	0.960	0.960	0.960
	$Accuracy_{pred}$	0.966	0.967	0.970	0.969	0.969	0.968
	$Precision_{pred}$	0.990	0.995	1.000	0.999	0.999	0.999
	$Recall_{pred}$	0.965	0.963	0.962	0.960	0.961	0.959
	Qualitative	1	2	2	3	4	4
	Computation time (s)	0.372	15.082	0.672	0.265	26.742	0.276
Geneva	Processing	Raw	Raw	Raw	Raw	Raw	Raw

	Neurons			2			
	$Accuracy_{cal}$	0.999	1.000	0.998	0.997	0.993	0.991
	$Precision_{cal}$	1.000	1.000	1.000	1.000	0.995	0.990
	$Recall_{cal}$	0.999	1.000	0.996	0.994	0.992	0.992
	$Accuracy_{pred}$	0.996	0.996	0.996	0.993	0.991	0.993
	$Precision_{pred}$	1.000	1.000	1.000	1.000	1.000	1.000
	$Recall_{pred}$	0.996	0.996	0.996	0.993	0.991	0.993
	Qualitative	2	2	4	4	4	4
	Computation time (s)	0.223	17.307	0.758	0.437	52.612	0.404

823